DRAFT VERSION AUGUST 21, 2025
Typeset using LaTeX **twocolumn** style in AASTeX631

Mid-infrared JWST spectra of carbon stars in the Large Magellanic Cloud

G. C. SLOAN,[1,2] B. ARINGER,[3,4] KATHLEEN E. KRAEMER,[5] J. CAMI,[6,7] K. ERIKSSON,[3] S. HÖFNER,[3] K. JUSTTANONT,[8] E. LAGADEC,[9] PAOLA MARIGO,[10,11] M. MATSUURA,[12] I. MCDONALD,[13] E. J. MONTIEL,[14,15] R. SAHAI,[16] AND A. A. ZIJLSTRA[13]

[1]*Space Telescope Science Institute, 3700 San Martin Drive, Baltimore, MD 21218, USA*
[2]*Department of Physics and Astronomy, University of North Carolina, Chapel Hill, NC 27599-3255, USA*
[3]*Theoretical Astrophysics, Department of Physics and Astronomy, Uppsala University, Box 516, 751 20 Uppsala, Sweden*
[4]*Department of Astrophysics, University of Vienna, Türkenschanzstraße 17, 1180 Wien, Austria*
[5]*Institute for Scientific Research, Boston College, 140 Commonwealth Avenue, Chestnut Hill, MA 02467, USA*
[6]*Department of Physics and Astronomy, The University of Western Ontario, London, ON N6A 3K7, Canada*
[7]*Institute for Earth and Space Exploration, The University of Western Ontario, London, ON N6A 3K7, Canada*
[8]*Chalmers University of Technology, Dept. Space, Earth and Environment, Onsala Space Observatory, 439 92 Onsala, Sweden*
[9]*Université Côte d'Azur, Observatoire de la Côte d'Azur, CNRS, Laboratoire Lagrange, Bd de l'Observatoire, CS 34229, 06304 Nice Cedex 4, France*
[10]*Department of Physics and Astronomy G. Galilei, University of Padova, Vicolo dellOsservatorio 3, I-35122 Padova, Italy*
[11]*Deceased*
[12]*Cardiff Hub for Astrophysical Research and Technology (CHART), School of Physics and Astronomy, Cardiff University, The Parade, Cardiff CF24 3AA, UK*
[13]*Jodrell Bank Centre for Astrophysics, The University of Manchester, Manchester, M13 9PL, UK*
[14]*U.S. Naval Observatory, 3450 Massachusetts Ave. NW, Washington, DC 20392, USA*
[15]*SOFIA-USRA, NASA Ames Research Center, MS 232-12, Moffett Field, CA, 94035, USA*
[16]*Jet Propulsion Laboratory, MS 183-900, 4800 Oak Grove Dr., California Institute of Technology, Pasadena, CA 91109, USA*

ABSTRACT

Mid-infrared spectra from the Medium-Resolution Spectrometer on the James Webb Space Telescope have revealed the molecular chemistry of carbon stars in the Large Magellanic Cloud in unprecedented detail. Our sample spans a range of dust-production rates and includes three relatively dust-free semi-regular variables and six dustier Mira variables. All were observed 15–20 years earlier with the Infrared Spectrograph on the Spitzer Space Telescope at lower spectral resolution. The new spectra show that the C_3 molecule is responsible for a strong absorption band centered at 5.2 μm. CS is clearly present in some of the sample, especially the stars with less dust. HCN also appears to be present. Some of the spectra have changed significantly between the Spitzer epoch and the current epoch, and in most cases, these changes can be attributed to the stellar pulsation cycle. One exception is the disappearance of a dust emission feature at $\sim$18 μm in one of the Miras. The new spectra confirm the existence of what resembles a broad absorption band from an unknown carrier centered at $\sim$10 μm, although we cannot rule out the possibility of molecular emission to either side of the apparent absorption. The presence of this spectral structure on the short-wavelength side of the SiC dust emission feature at $\sim$11.3 μm combined with the broad C_2H_2 band centered at 14 μm raise the possibility that some previously reported detections of weak SiC dust emission in other carbon stars may not be real.

Keywords: carbon stars (199); asymptotic giant branch stars (2100); long period variable stars (935); circumstellar dust (236); circumstellar gas (238)

1. INTRODUCTION

Carbon stars dominate the population of evolved stars on the asymptotic giant branch (AGB) in the nearby Large and Small Magellanic Clouds (LMC and SMC; Blanco et al. 1978, 1980; Cioni & Habing 2003). They also dominate the production of dust in these metal-poor dwarf galaxies (Matsuura et al. 2009, 2013; Boyer et al. 2012; Srinivasan et al. 2016). AGB stars turn carbon-rich when they produce carbon via the triple-α process (Salpeter 1952) and dredge enough of it up to their surfaces to push the C/O ratio above 1.0 (Renzini & Voli 1981). These stars

Corresponding author: G. C. Sloan
gcsloan@stsci.edu

are unstable to pulsations in their envelopes which trigger the mass loss that will strip them to their cores (e.g., Habing 1996; Mattsson et al. 2008; Liljegren et al. 2016; Höfner & Olofsson 2018).

Kraemer et al. (2019) showed that the amplitude of the pulsations is critical to the quantity and chemistry of the dust produced (see also McDonald & Trabucchi 2019). Carbon stars pulsating weakly as semi-regular variables (SRVs) form small amounts of dust dominated by SiC. Carbon stars pulsating strongly enough to be classified as Mira variables produce significantly higher amounts of dust, primarily amorphous carbon, which dominates the dust as the stars evolve (Martin & Rogers 1987). Once a carbon star is forming amorphous carbon, the grains are opaque enough to be accelerated to escape velocity by radiation pressure from the central star and drag the gas along with it (e.g., Wickramasinghe et al. 1966; Woitke 2006; Mattsson et al. 2010; Bladh et al. 2019; Eriksson et al. 2023).

The dust condenses from molecular gas in the atmosphere, but a clear understanding of the molecular chemistry is lacking. Cherchneff et al. (2006) provide a good map of the reaction pathways and compounds to be expected. In a carbon-rich atmosphere, CO consumes all of the available oxygen, and molecules such as C_2H_2, HCN, SiS, and CS will form. All four have been identified in the mid-infrared spectra of Galactic carbon stars (Aoki et al. 1998, 1999), using the Short Wavelength Spectrometer (SWS; de Graauw et al. 1996; Leech et al. 2003) aboard the Infrared Space Observatory (ISO; Kessler et al. 1996, 2003). Acetylene (C_2H_2) may be the primary building block of the benzene molecule (C_6H_6; Frenklach & Feigelson 1989), which in turn is the building block of graphite, amorphous carbon, and polycyclic aromatic hydrocarbons (PAHs; e.g., Allamandola et al. 1989).

The launch of the Spitzer Space Telescope (Werner et al. 2004) made it possible to obtain sizable mid-infrared spectroscopic samples of carbon stars in nearby galaxies in the Local Group, which enabled the study of how metallicity affects the photospheric chemistry and the production of dust in carbon stars. Using the Infrared Spectrograph (IRS) on Spitzer (Houck et al. 2004), several studies obtained spectra of a total of 184 carbon stars in the Large Magellanic Cloud (LMC; see Sloan et al. 2016, and references therein). The LMC has a metallicity which ranges between 30 and 50% Solar ($-0.5 < \mathrm{[Fe/H]} < -0.3$) (Piatti & Geisler 2013; Choudhury et al. 2016). Despite the difference in metallicity, carbon stars in the LMC and even the more metal-poor SMC showed no notable differences in the quantity of dust produced compared to a sample of Galactic carbon stars observed by the SWS on ISO (Sloan et al. 2008). This trend continues to carbon stars in even more metal-poor dwarf spheroidal galaxies in the Local Group (Sloan et al. 2012). These results attest to the power of helium-burning and dredge-ups on the AGB. Carbon stars are producing all the carbon they need to make dust themselves, no matter their initial metallicity. Thus, they are likely contributors to the dust in galaxies even in the high-redshift Universe.

While metallicity does not affect the dust-production rates in carbon stars strongly, the molecular component is another matter. In Galactic carbon stars, acetylene, HCN, CS, and SiS are all detected in the mid-infrared, but in the LMC and SMC, only acetylene has been observed (Aoki et al. 1998; Matsuura et al. 2006). This difference could arise from the lower metallicities of the stars, but the IRS spectra have a spectral resolving power ($R \equiv \lambda/\Delta\lambda$) of $\sim$100, which is high enough to study the molecular bands as a whole but too low to study the detailed structure within them. Thus, it is possible that low levels of absorption from molecules beside acetylene were present but went undetected.

This project follows up on carbon stars in the LMC previously observed with the IRS on Spitzer to better understand the nature of the molecular absorption in their spectra. We have observed a sample of carbon stars in the LMC with the Medium-Resolution Spectrometer (MRS; Wells et al. 2015), an observing mode of the Mid-Infrared Instrument (MIRI; Wright et al. 2023) aboard the James Webb Space Telescope (JWST; Gardner et al. 2023). The first three spectra in the sample observed with the MRS raised temporal variations as another dynamic to be considered (Sloan et al. 2024).

This paper presents an overview of the entire sample and focuses on (1) qualitative molecular analysis, (2) temporal spectral variations, and (3) their relation to the stellar pulsation cycles. Section 2 introduces the sample of spectroscopic targets, Section 3 describes the observations and data reduction, and Section 4 presents the results of the spectral analysis. Sections 5 and 6 discuss and summarize the results. The appendices examine the ancillary data used in this paper and supplement the figures from the spectral analysis.

2. SAMPLE

JWST program 3010 observed nine carbon stars in the LMC with the MRS on MIRI in Cycle 2. Table 1 provides details on the properties and observations of each star. Figure 1 plots the sample along with all carbon-rich Mira variables and SRVs from the Optical Gravitational Lensing survey of the LMC (OGLE-III; Soszyński et al. 2009). The photometry comes from the Infrared Array Camera on Spitzer (IRAC; Fazio et al. 2004), the Wide-field Infrared Survey Explorer (WISE; Wright et al. 2010), and the Near-Earth Object WISE Reactivated mission (NEOWISE-R; Mainzer et al. 2014). The data in the 3.4 and 4.6 μm WISE filters (W1 and

Table 1. The MRS sample of carbon stars in the LMC

Target[a]	RA (J2000)	Declination (J2000)	Var. type	Period (days)[b]	Luminosity ($L_\odot$)[c]	[3.6]−[4.5] (mag)[d]	Integration time (s)	IRS epoch (MJD)	MRS epoch (MJD)
J050629	76.623347	−68.926346	SRV	(218)	3820 ± 3	−0.150	5784	54484	60273
KDM 1691	75.903917	−68.560699	SRV	523	13650 ± 560	−0.094	1340	54649	60551
WBP 17	81.582833	−69.693703	SRV	309	5510 ± 310	−0.034	4224	53596	60551
WBP 29	81.670642	−69.386490	Mira	245	5010 ± 50	0.076	5112	53482	60274
J051803	79.513592	−68.830750	Mira	372	3270 ± 300	0.323	1560	54688	60490
J053441	83.672587	−69.441864	Mira	519	9190 ± 590	0.643	540	54611	60551
MSX LMC 220	78.133621	−69.261230	Mira	637	15760 ± 530	0.863	540	53379	60551
MSX LMC 774	81.596238	−69.188965	Mira	671	8180 ± 720	1.134	540	53445	60551
MSX LMC 736	83.278350	−70.509682	Mira	690	8210 ± 620	1.375	628	54611	60385

[a] The three stars with names beginning with "J" have the more formal coordinate-based names 2MASS J0506290−6855348, SSTISAGE1C J051803.23−684950.7, and 2MASS J05344142−6926307. This paper will refer to them by their shorter "J" names throughout.

[b] See Appendix A. Values in parentheses are uncertain.

[c] See Appendix B.

[d] From photometry reported by Sloan et al. (2016).

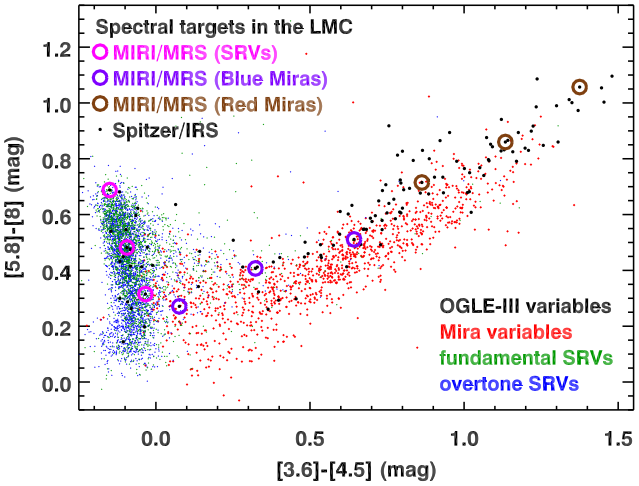

Figure 1. The sample of nine MRS targets (open circles) in color-color space defined by the four IRAC filters, plotted with data from the OGLE-III sample of carbon-rich long-period variables in the LMC (Soszyński et al. 2009) and the carbon stars observed by the IRS on Spitzer (Sloan et al. 2016). Three of the targets sample the SRV sequence (magenta), and the other six cover the Mira sequence (purple and brown).

W2) have been shifted to the IRAC 3.6 and 4.5 μm filters using the conversions from Sloan et al. (2016).

The colors of the carbon stars follow two distinct sequences. The Mira variables, which are undergoing strong fundamental-mode pulsations in their atmospheres, lie to the right of the boundary at [3.6]−[4.5] ∼ 0. The SRVs lie to the left of that boundary, no matter their pulsation mode. The range of [5.8]−[8] colors in the SRVs probably arises from varying strengths of molecular absorption bands in their spectra. Molecular absorption may redden the color by preferentially decreasing the emission in the 5.8 μm filter, and C_3 is a likely suspect (Sloan et al. 2015). In the Mira variables, on the other hand, the increasing red colors in all filters result from higher optical depths of amorphous carbon dust around them.

We selected nine targets in Program 3010 to track both the SRV and Mira sequences in Figure 1, with three stars along the SRV sequence and six along the Mira sequence. We chose targets that had been previously observed by the IRS on Spitzer, were roughly evenly spaced along the two sequences, and were close to the bar of the LMC so that they were observed in six epochs with IRAC on Spitzer. The first two IRAC epochs were from the program Surveying the Agents of a Galaxy's Evolution, which surveyed the entire LMC (SAGE; Meixner et al. 2006). The other four epochs were obtained in the SAGE-Var program (Riebel et al. 2015).

Figure 1 shows the Spitzer/IRS sample of carbon stars in the LMC as black dots. The nine sources also observed by the MRS on JWST are circled in magenta (for the SRVs) and purple and brown (for the bluer and redder Miras, respectively).

Table 1 provides the pulsation periods and luminosities of the stars in the sample, which were determined as described in Appendices A and B, respectively. Figure 2 compares the properties of the sample to evolutionary tracks from Vassiliadis & Wood (1993), which gives a rough idea of the

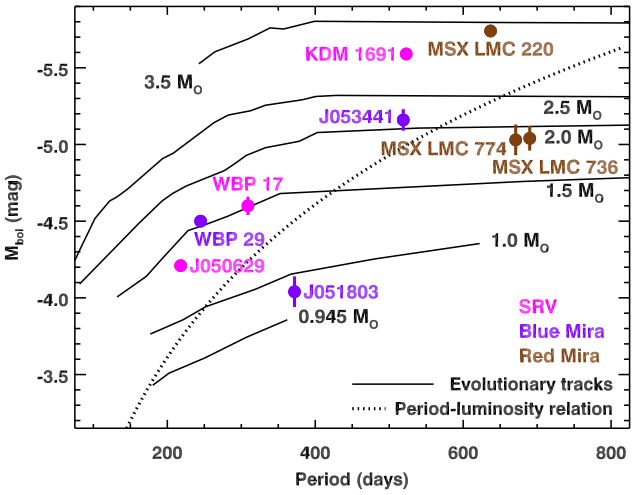

Figure 2. The stars in our sample compared to evolutionary tracks by Vassiliadis & Wood (1993) and the period-luminosity relation for carbon stars (Whitelock et al. 2009). Appendix B decribes how the luminosities were calculated.

initial mass of the stars. KDM 1691 and MSX LMC 220 are significantly more luminous than the rest of the sample, and thus more massive and in all likelihood more metal-rich. J051803 appears to be the least massive and therefore oldest and most metal-poor star in the sample. The SRVs are all to the left of the period-luminosity relation determined by Whitelock et al. (2009), which is arguably consistent with overtone pulsation modes, but the spread in the Miras to either side of the relation indicates that the relation must be broad and not well defined by a single curve.

3. OBSERVATIONS AND DATA REDUCTION

Each of the nine stars in the sample was observed in all three grating settings in the MRS, giving complete coverage at a spectral resolving power of ∼2000–3000 from 4.9 to 28 μm, although the data cease to be meaningful past a limit of ∼19–22 μm, depending on the brightness of the star. Integration times were set to achieve a minimum signal/noise ratio (S/N) of ∼100 from 5 to 12 μm. For the reddest three stars in the sample, the S/N stayed above ∼100 out to ∼18 μm. Each target was observed with the four-point dither pattern optimized for point sources in all MRS channels.

The spectral data were processed using the JWST pipeline version 1.18.0 and Calibration Data Reference System (CRDS) context jwst_1364.pmap. This version of the pipeline processed the 12 spectral segments (four channels, three grating segments) separately and applied the optional residual defringing algorithm to each. The flux calibration produces results within 1% of the IRS on Spitzer for standard stars observed by both (Law et al. 2024). Figures 3 to 5 present the resulting spectra from the MRS and compare them to the IRS.

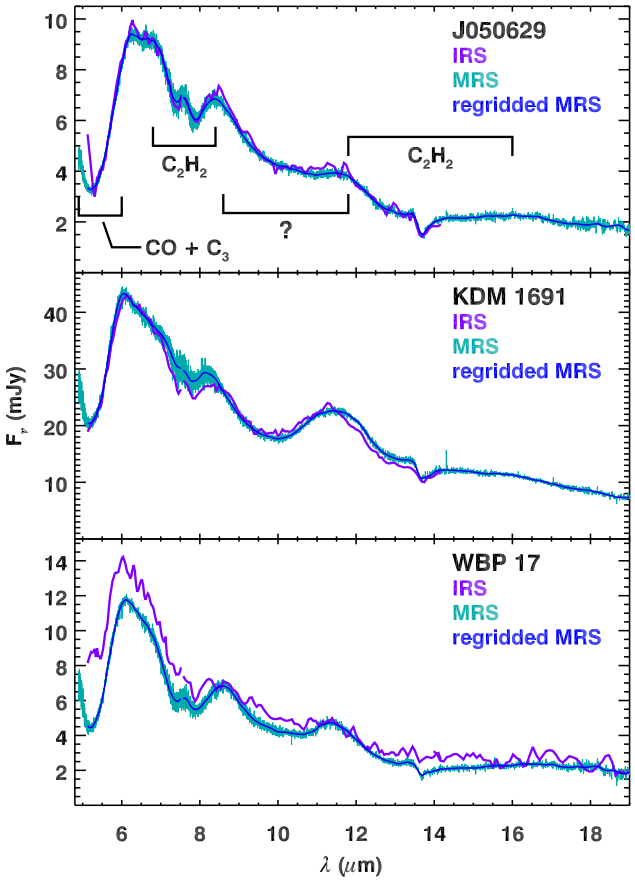

Figure 3. MRS spectra of the three semi-regular variables, compared to the spectra from the IRS. The spectra from the MRS are plotted as produced by the pipeline and also after regridding them to the lower-resolution wavelength grid of the IRS.

4. SPECTRAL ANALYSIS

4.1. *The Manchester Method*

We have measured the strength of the acetylene absorption band at 7.5 μm and the SiC dust feature at ∼11.5 μm using the Manchester Method, which estimates the continuum by fitting a line segment to either side of the spectral features. Sloan et al. (2016) describe this method and its history (see their Figures 1–2 for illustrations). While the Manchester Method is arguably simplistic, it does provide a quick measurement using a method applied to hundreds of other carbon-star spectra for comparison. It also provides a color in two discrete wavelength bands centered at 6.4 and 9.3 μm, which sample spectral regions that come closer to continuum than most others in these complex spectra. The "continuum" in these spectra is a combination of emission from the star and amorphous carbon dust, which has no resonances and thus no spectral features in the infrared. The [6.4]−[9.3] color measures the amount of amorphous carbon dust around the star, with higher dust-production rates leading to increasingly red colors (Groenewegen et al. 2007).

Table 2. Spectroscopic data

	[6.4]−[9.3]	C_2H_2 at 7.5 μm		SiC dust emission	
Target	(mag)	Wavelength (μm)[a]	Eq. width (μm)[b]	Wavelength (μm)[a]	SiC/continuum[bc]
J050629	0.144 ± 0.003	7.67 ± 0.01	0.155 ± 0.001	11.55 ± 0.01	(0.097 ± 0.001)
KDM 1691	0.031 ± 0.002	7.51 ± 0.01	0.102 ± 0.001	11.38 ± 0.01	0.238 ± 0.001
WBP 17	−0.001 ± 0.004	7.46 ± 0.00	0.335 ± 0.001	11.42 ± 0.01	0.180 ± 0.001
WBP 29	−0.130 ± 0.003	7.41 ± 0.02	0.012 ± 0.001	12.17 ± 0.03	(0.023 ± 0.002)
J051803	0.452 ± 0.001	7.48 ± 0.01	0.106 ± 0.001	11.08 ± 0.02	(0.038 ± 0.000)
J053441	0.452 ± 0.001	7.45 ± 0.00	0.122 ± 0.001	11.27 ± 0.02	0.045 ± 0.001
MSX LMC 220	0.830 ± 0.001	7.54 ± 0.02	0.039 ± 0.001	11.33 ± 0.01	0.090 ± 0.001
MSX LMC 774	0.908 ± 0.001	7.48 ± 0.00	0.107 ± 0.001	11.29 ± 0.01	0.141 ± 0.001
MSX LMC 736	1.147 ± 0.001	7.56 ± 0.01	0.133 ± 0.001	11.33 ± 0.01	0.155 ± 0.001

[a] The central wavelength of the band or feature as defined in the text.

[b] Uncertainties are lower limits; they do not account for systematic effects, as Section 4.1 explains.

[c] Questionable measurements are in parentheses.

Table 2 gives the results for the [6.4]−[9.3] color, the equivalent width of the acetylene absorption at 7.5 μm, and the strength of the SiC dust emission feature at ∼11.3 μm with respect to the continuum. Figures 6 and 7 plot the strengths of the acetylene absorption and SiC emission versus the [6.4]−[9.3]. Both figures exclude the eight deeply reddened carbon stars observed with the IRS in the LMC with [6.4]−[9.3] > 2.0.

For the absorption band and the dust emission, Table 2 reports a central wavelength, defined as the wavelength which bisects the absorption or emission. It provides a useful check of the extracted feature. All of the acetylene bands have central wavelengths between 7.4 and 7.7 μm and appear to be valid, even the weak band in WBP 29.

The central wavelength of the extracted feature rules out the presence of SiC dust emission in the spectra of WBP 29 and J050629, based on a comparison to the sample of carbon stars in the LMC published by Sloan et al. (2016). That sample includes 123 sources with a SiC/continuum ratio > 0.05 (out of 184). The mean central wavelength = 11.293 ± 0.113. Taking two standard deviations to define the range of valid central wavelengths gives 11.07–11.52 μm. Both WBP 29 and J050629 are outside this range. One other source, J051803, is close to blue edge, faint, and therefore also questionable.

The uncertainties in the strengths of the extracted features in Table 2 are statistical. They should be treated as lower limits, because they do not include the systematic effects from how spectral structure (from molecular bands or solid-state features) on either side of the band or feature considered might affect the continuum. In the case of the SiC dust emission feature, absorption from C_2H_2 to the red will affect the measured strength. Thus, a high ratio of feature strength to uncertainty does not necessarily mean the feature is real.

4.2. *Analysis of the detailed molecular band structure*

The analysis uses a grid of synthetic spectra based on hydrostatic models with effective temperatures of 3100 K and 2800 K, a range of C/O ratios from 1.05 to 4.0, M = 1.0 $M_\odot$, log g (cm s^{-2}) = 0.0, and a metallicity ([Z/H]) of −0.5. The models are based on the COMARCS code (Aringer et al. 2016, 2019). The models used EXOMOL line lists for C_2H_2 (Chubb et al. 2020), C_3 (Lynas-Gray et al. 2024), HCN (Harris et al. 2008; Barber et al. 2014), and CS (Paulose et al. 2015), and the HITEMP line list for CO (Li et al. 2015)[1]. The models include isotopologues of the above molecules (at solar abundances), other molecules, and atomic transitions.

The hydrostatic models provide synthetic spectra with detailed band structure for individual molecules which can greatly aid the identification of what is absorbing in different wavelength regions. The hydrostatic models do not include pulsation, convective structures, or winds and as a consequence will not include the cooler layers of gas likely to be responsible for much of the observed molecular spectral structure. As a result, we should not expect the band depths or the relative strengths of the available transitions in the synthetic spectra to match the observed spectra. The

[1] https://hitran.org/hitemp

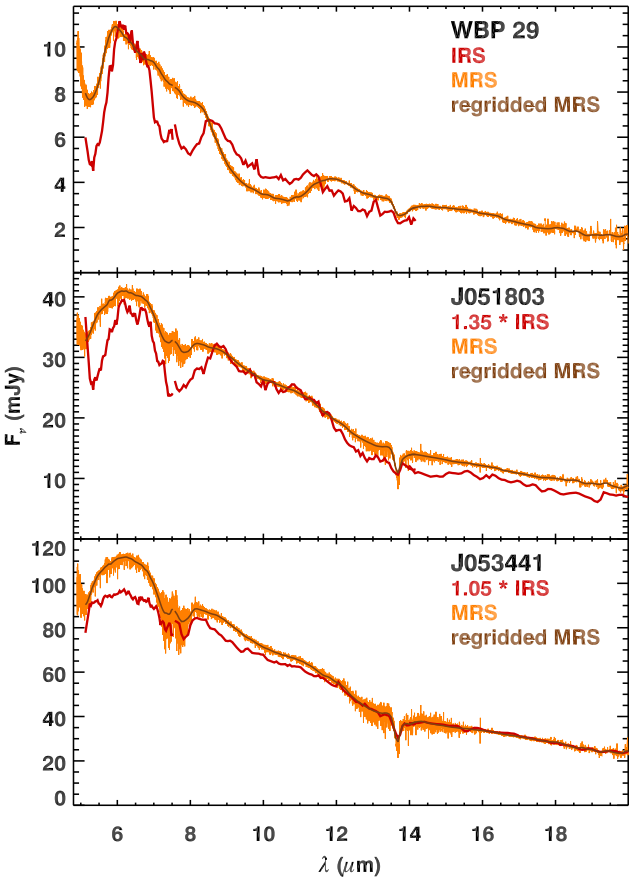

Figure 4. MRS spectra of the three bluest of the six Mira variables, compared to the spectra from the IRS. As in Figure 3, the spectra from the MRS are plotted before and after regridding to the IRS. Two of the IRS spectra have been scaled up multiplicatively to match the brightness of the MRS spectra to make comparisons easier.

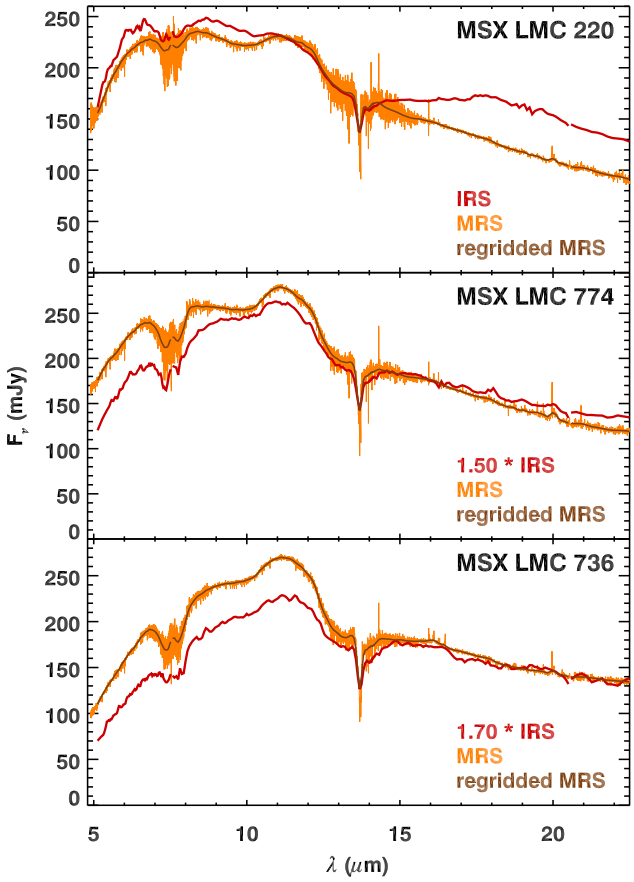

Figure 5. MRS spectra of the three reddest Mira variables, compared to the spectra from the IRS. As in Figure 4, the MRS spectra are plotted before and after regridding, and two of the IRS spectra have been shifted up to align with the MRS.

present analysis focuses on the detailed spectral structure within short wavelength intervals rather than attempting to model the overall band strength and shape. With the exception of measuring radial velocities, the analysis is more qualitative than quantitative.

We confine the spectral analysis in this work to what can be described as the "flatten-and-fit" method. We have broken the spectra into multiple wavelength intervals, with intervals at 4.9–5.2 and 5.2–5.5 μm to investigate absorption by CO and C_3, 7.0–7.5, 7.5–8.0, and 8.1–8.6 μm for C_2H_2, HCN, and CS, and 12.6–13.1, 13.1–13.6, and 13.8–14.3 μm for C_2H_2 and HCN.

In each interval, we take the following steps: (1) create a pseudo-continuum from the observed spectrum by generating a median with a 100-pixel interval, (2) divide the spectrum by that pseudo-continuum to isolate the spectral structure within the band, and (3) subtract 1.0 so that the spectral emission and absorption structure oscillates around a mean value of 0.0. The pseudo-continuum runs through the middle of the band structure and not the top, as might be more appropriate for an absorption spectrum. The synthetic molecular absorption spectra follow the same steps, except that we initially downsampled them to the wavelength grid and resolution of the MRS, using the resolutions as defined by Pontoppidan et al. (2024). When fitting the synthetic absorption to an observed spectrum, we normalize the synthetic spectrum to the mean of the absolute value of the observed spectrum across a wavelength interval. The acetylene band at 7.5 μm flattens pretty well, but the deep and narrow Q branch from the ν_5 band at 13.7 μm retains some of its structure, which is why the chosen intervals skip from 13.6 to 13.8 μm. We placed the 8 μm interval at 8.1–8.6 μm to concentrate on the region where CS absorbs most strongly.

4.2.1. *Radial velocities*

To determine the radial velocities of the stars in the sample, we iterated in 1 km/s steps from 160 to 320 km/s and also through different mixtures of the 2–3 molecules contributing

Table 3. Radial velocities

Target	$T_{\rm eff}$ (K)	Radial velocity (km/s) in wavelength interval (μm)[a] 4.9–5.2	5.2–5.5	7.0–7.5	7.5–8.0	8.1–8.6	12.6–13.1	13.1–13.6	13.8–14.3	Mean rad. vel. (km/s)[b]
J050629	3100	244	(184)	229	250	240	(180)	248	(263)	242 ± 4
KDM 1691	3100	278	270	260	266	261	239	277	(183)	264 ± 5
WBP 17	3100	289	270	261	268	261	238	277	266	266 ± 5
WBP 29	2800	240	229	224	240	(238)	(180)	228	247	235 ± 4
J051803	2800	241	179	224	204	(271)	(180)	223	(235)	214 ± 11
J053441	2800	244	(226)	224	204	(275)	(180)	223	(228)	224 ± 8
MSX LMC 220	2800	240	184	213	203	240	(178)	206	(183)	214 ± 9
MSX LMC 774	2800	241	221	234	227	(276)	(180)	221	(183)	229 ± 4
MSX LMC 736	2800	277	226	224	206	(278)	189	258	(316)	230 ± 13

[a] Velocities in parentheses were not used.

[b] Uncertainties are uncertainties in the mean.

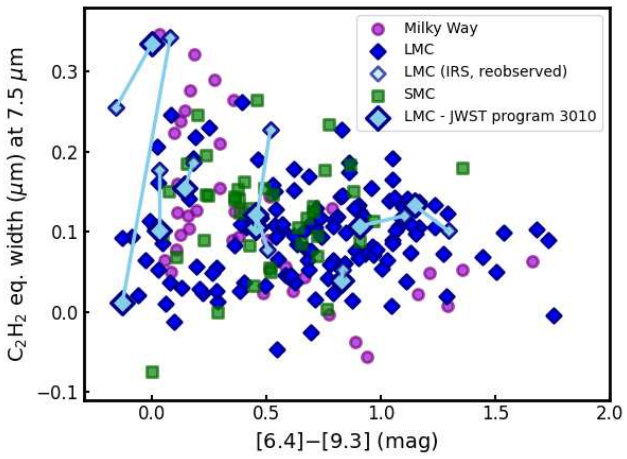

Figure 6. The equivalent width of the 7.5 μm acetylene absorption band as a function of the [6.4]−[9.3] color. The nine stars in the present sample are plotted as small light-blue diamonds as observed by the IRS and large light-blue diamonds as observed by the MRS. WBP 29 has moved dramatically from top left to bottom left due to its disappearing acetylene band.

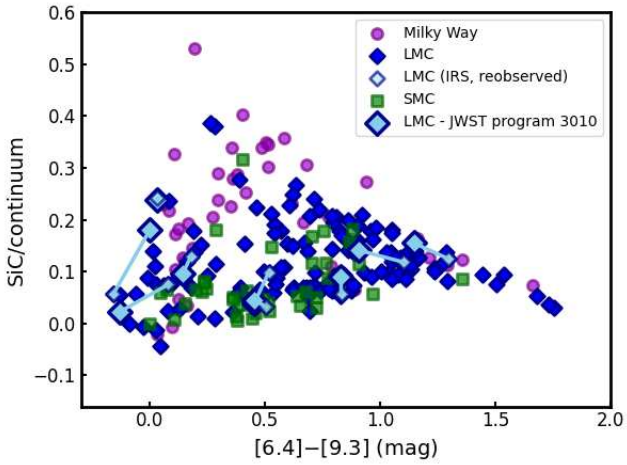

Figure 7. The strength of the SiC dust emission feature versus the [6.4]−[9.3] color, with IRS and MRS results plotted as in Figure 6.

to each wavelength interval. Generally, the best radial velocity depended only weakly on the details of the chemical mixture. For the SRVs, we chose an effective temperature $T_{\rm eff}$ = 3100 K, and for the Miras, 2800 K. For all stars, we used synthetic spectra based on models with a C/O ratio = 2.0.

Table 3 gives the resulting radial velocities for each star in each wavelength interval. The 8.1–8.6 μm interval presented problems in the Mira variables, with the χ^2 residuals not presenting well-defined minimum in most cases. The 12.6–13.1 and 13.8–14.3 μm intervals were also difficult, leading us to use the fitted radial velocities in only the best behaved cases. We rejected two of the fitted velocities in the 5.2–5.5 μm for the same reason.

For a given star, the apparent velocities can vary significantly between intervals, possibly because of noise in the data and the caveats listed below. Another possibility is that some of the differences could be real, as different molecules could be tracing different layers in the pulsating stellar atmosphere. Even for the same molecule, absorption at different wavelengths could arise from gas at different opacities and thus different temperatures and layers. Nonetheless, we are able to determine radial velocities with uncertainties less than 10 km/s in most cases.

Comparing our radial velocities to those from Gaia DR3 increases our confidence in the results (Gaia Collaboration

2016, 2023). Gaia has radial velocities for three stars in our sample. For KDM 1691, Gaia gives v_{rad} = 260 ± 1 km/s, compared to the MRS result of 264 ± 5 km/s. For WBP 17, v_{rad} = 261 ± from Gaia and 266 ± 5 from the MRS, and for WBP 29, the corresponding results are v_{rad} = 240 ± 3 and 235 ± 4. In all three cases, the error bars overlap.

This procedure comes with a number of caveats. The only molecules we considered were CO, C_3, C_2H_2, HCN, and CS (and not their isotopologues). Other molecules are certainly contributing to the spectra, As already noted, the spectra show evidence of absorption from molecules much cooler than one might expect in a hydrostatic model, and that difference in temperature could shift relative line strengths within bands and thus the apparent radial velocity. That motivated us to break broader spectral regions into smaller wavelength intervals, which reduces the effect of an incorrect temperature over larger wavelength ranges. Finally, the line lists may have errors in predicted line positions and intensities, which will increase the residuals in the fitting process.

4.2.2. *General results*

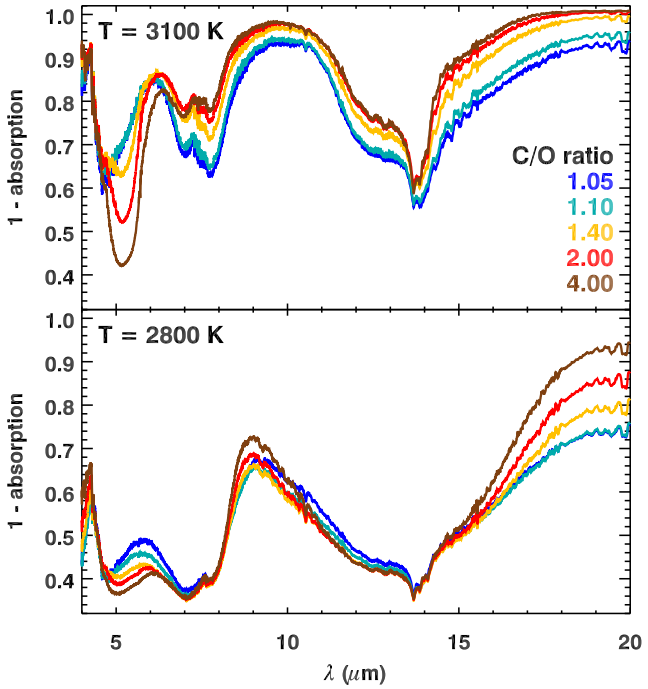

Figure 8. The absorption in the synthetic spectra based on hydrostatic models at two temperatues and five C/O ratios. The models have been regridded to the MRS wavelength grid and then smoothed with a 29-pixel boxcar. The 2800 K models show that the spectra are never even close to a real continuum in the mid-infrared.

Figure 8 plots synthetic spectra from the hydrostatic models at T_{eff} = 2800 K and 3100 K at five different C/O ratios. The synthetic spectra are normalized relative to a continuum taken from a calculation without any line opacities. The most important takeaway is in the 2800 K models, where the absorption is substantial throughout the mid-infrared. The spectra are nowhere near a true continuum level anywhere between 5 and 17 μm. That behavior illustrates how the Manchester Method is making broad assumptions about what can be used for a local "continuum."

In most cases in Figure 8, the acetylene absorption band at 7.5 μm in the synthetic spectra does not have the classic "W" shape seen in the observed spectra. This shape is apparent in the downsampled MRS spectra of all six Miras in Figure 4 and 5, but it is less obvious in the synthetic spectra, especially those based on the 2800 K models. In the hydrostatic models, the C_2H_2 aborption occurs in a layer with a temperature of ∼1200–1500 K, but to reproduce the "W" shape, the absorbing gas needs to be below 1000 K. Matsuura et al. (2006) were able to reproduce the band shape with a slab of absorbing C_2H_2 at 500 K. They also noted that the observed C_2H_2 absorption at 13.7 μm in carbon stars heavily obscured by circumstellar dust requires that the absorbing gas be above the dust photosphere, which would be in the circumstellar envelope and well above the stellar photosphere. Hydrostatic models do not reproduce this structure, which is why the present analysis is limited to the flattening-and-fitting method.

Table 4 presents the results of our analysis of the flattened spectra, where we have fitted the relative molecular contributions in the smaller wavelength intervals listed in Table 3 and combined the results into groups of wavelength intervals. Where a molecule clearly dominates the absorption, it is in bold type. Otherwise, the order of the molecules listed is not significant. Analysis based on more realistic models would be required for quantatively meaningful relative abundances. Appendix C plots the best-fitting models in each wavelength interval for each star.

4.2.3. *C_3 and CO at 5 μm*

Figure 9 compares the observed spectra of the SRVs with synthetic spectra based on 3100 K models after the spectra have been smoothed with a 29-pixel boxcar. The spectra of the SRVs all show a minimum at ∼5.2 μm, and that matches the shape of the C_3 band in the synthetic spectra. The CO band, on the other hand, has a bandhead further to the blue at ∼4.6 μm. The synthetic spectra show that the C_3 band increases in strength as the C/O ratio increases, and it also grows wider. As in Figure 8, the absorptions in the synthetic spectra are based on ratios to synthetic spectra of models computed without line opacities.

Figure 10 looks more closely at the detailed band structure in the SRVs and compares it to absorption from C_3 and CO in synthetic spectra based on models with T_{eff} = 3100 K and

Table 4. Identified molecules

	Identified molecules in wavelength range[a]			
Target	5 μm	7–8 μm	8.1–8.6 μm	13–14 μm
J050629	**C_3**, CO	**C_2H_2**, HCN, CS	**CS**, C_2H_2	**C_2H_2**, HCN
KDM 1691	**C_3**, CO	C_2H_2, HCN, CS	**CS**	**C_2H_2**, HCN
WBP 17	**C_3**, CO	C_2H_2, HCN, CS	**CS**, HCN	**C_2H_2**, HCN
WBP 29	**C_3**, CO	C_2H_2, HCN, CS	**HCN**	**C_2H_2**, HCN
J051803	**C_3**, CO	**C_2H_2**, HCN, CS	**CS**	**C_2H_2**, HCN
J053441	**C_3**, CO	**C_2H_2**, HCN, CS	**CS**	**C_2H_2**, HCN
MSX LMC 220	**C_3**, CO	**C_2H_2**, HCN, CS	HCN, CS	**C_2H_2**, HCN
MSX LMC 774	**C_3**, CO	**C_2H_2**, HCN, CS	**CS**, HCN	**C_2H_2**, HCN
MSX LMC 736	**CO**, C_3	**C_2H_2**, HCN, CS	**CS**, HCN	**C_2H_2**, HCN

[a] Dominant molecules are in **bold**. Otherwise, the order is not significant.

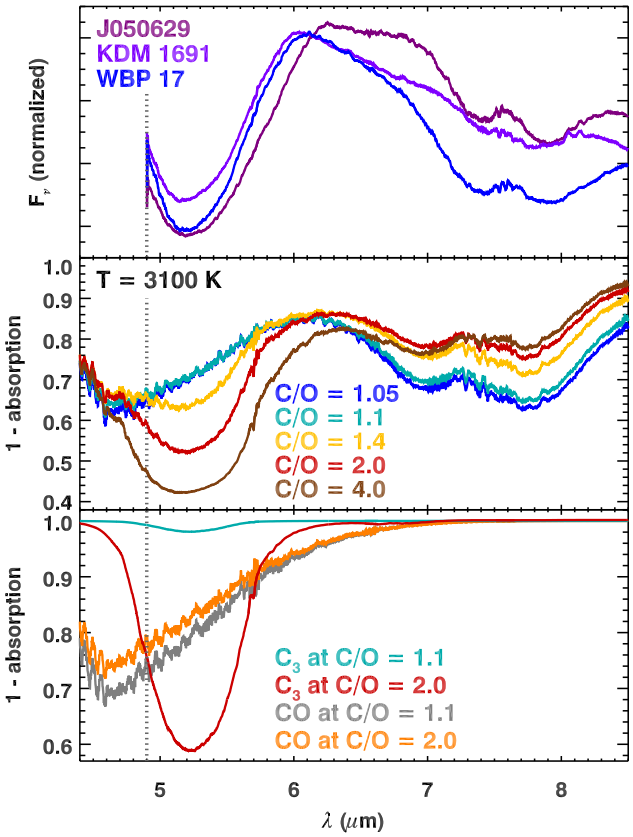

Figure 9. Observed spectra of the SRVs compared to absorption in the synthetic spectra from 4.4 to 8.5 μm at low spectral resolution. The MRS spectra and synthetic spectra have been smoothed with a 29-pixel boxcar. The vertical dotted line at 4.9 μm marks the blue edge of the MRS data. *Top:* Observed MRS data. *Middle:* Full absorption of all molecules and atoms considered in the models at $T_{\rm eff}$ = 3100 K. *Bottom:* Absorption from C_3 and CO.

C/O = 2.0. The observed spectra agree well with the synthetic

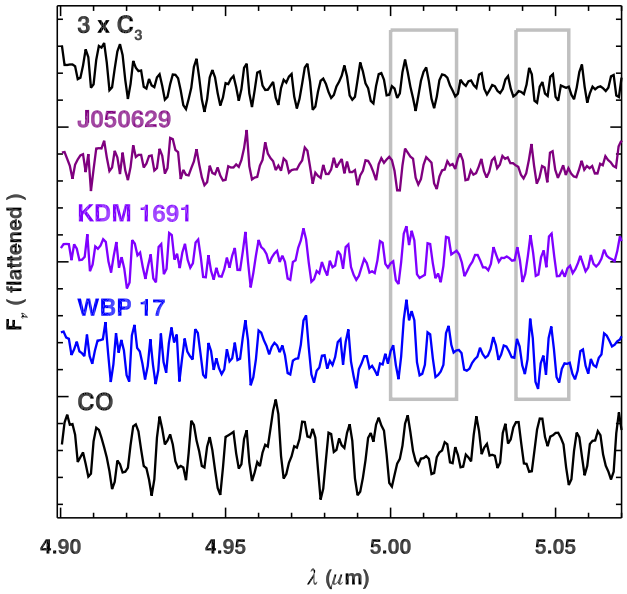

Figure 10. A comparison of the band structure of C_3 and CO to the flattened spectra of the SRVs between 4.9 and 5.07 μm. The gray boxes highlight two spectral regions with the clearest signal from C_3 in the observed spectra. The synthetic spectra (black) are for $T_{\rm eff}$ = 3100 K and C/O = 2.0.

absorption of C_3, confirming its presence, if not dominance, in the SRVs. The overall shape of the band in Figure 9 reinforces this conclusion. The analysis of the flattened spectra reveals that adding CO absorption reduces the residuals, and roughly speaking, the fraction of CO required increases as one moves from the SRVs to the bluer Miras to the redder Miras. For the reddest target, MSX LMC 736, only CO is needed in the 4.9–5.2 μm region. The figures in Appendix C show these results in more detail and for the Miras.

The low-resolution spectra from the IRS typically cease to be meaningful below 5.1 μm, while the MRS data are good

to 4.9 μm. The additional 0.2 μm greatly help our ability to identify C_3, as the upturn below the peak absorption at 5.2 μm is unambiguous. Figures 3 to 5 show that C_3 is clearly present in the three SRVs and the three blue Miras, but not as obvious in the three red Miras.

Comparing the spectra from the MRS to the synthetic spectra confirms previous hypotheses that C_3 explains the range of reddening in the [5.8]−[8] color in the SRVs, which can be seen in Figure 1. The synthetic spectra suggest further that the cause of the varying quantities of C_3 may be the C/O ratio in the atmosphere of the SRV. However, this conclusion is only qualitative due to the limits of the hydrostatic models. The actual C/O values needed to reproduce the depth and shape of the observed C_3 band require further investigation.

4.2.4. *CS at 8 μm*

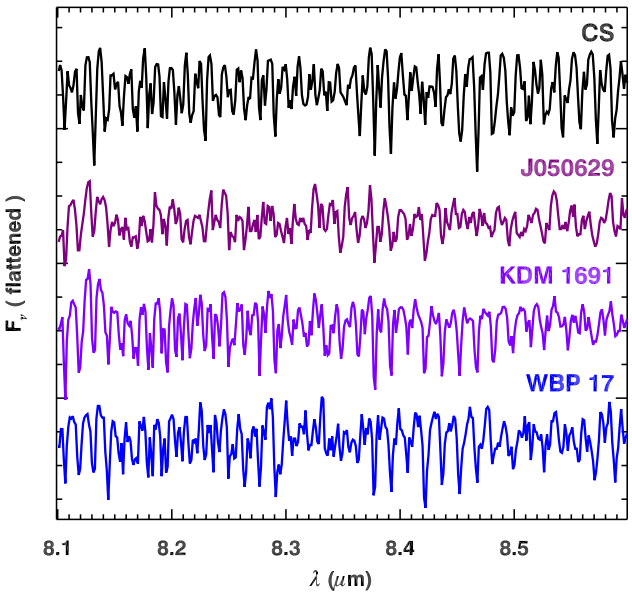

Figure 11. The 8.1–8.6 μm spectra of the three SRVs (in color) and the synthetic spectrum of CS from the hydrostatic model at 3100 K and C/O = 2.0 (black). CS is clearly present in KDM 1691 and WBP 17, and while less visible in J050629, is required to minimize the residuals.

Figure 11 compares the 8.1–8.6 μm spectra of the three SRVs with CS from the synthetic spectrum from a 3100 K model with C/O = 2.0. The presence of CS is unmistakable in all three spectra. The other possible contributors, C_2H_2 and HCN, have different spectral signatures in this wavelength interval, as can be seen in the spectra in Appendix C. The spectra in Appendix C reveal that CS is present in the SRVs in the 7.5–8.0 μm interval, too. Thus, the MRS and its higher spectral resolution can detect CS while the lower resolution of the IRS on Spitzer ($R \sim 100$) could not (Matsuura et al. 2006).

4.2.5. *HCN*

Matsuura et al. (2006) did find evidence of HCN in one or two Magellanic carbon stars in their low-resolution IRS spectra. The spectra from the MRS present stronger evidence, but no clear proof like that found for C_3 or CS. The iterative fitting process of the flattened spectra found, for all nine stars in the sample, that the presence of HCN results in lower χ^2 residuals in most or all of the wavelength intervals from 7.0 to 14.3 μm. The figures in Appendix C compare the observed spectra with HCN and other possible contributors. Thus, while the evidence for HCN is not conclusive, it is strong.

5. DISCUSSION

5.1. *WBP 29 and spectral variations in the sample*

While WBP 29 is classified as a Mira variable, it lies close in color-color space to the boundary with the SRVs (Figure 1). Its pulsational properties separate it from the other Miras. It has the shortest pulsational period of the Miras, and, for the Miras where we have measured the pulsation amplitudes with confidence, it has the lowest amplitude (Table 6 in Appendix A).

WBP 29 may be in transition from an SRV to a Mira, and its spectrum has changed dramatically between the IRS and MRS epochs, with the 7.5 μm acetylene band almost disappearing and an apparent 10 μm absorption band growing strong in its place (Figure 4). Sloan et al. (2024) raised the possibility that the changes in its spectral properties could be due to evolutionary changes in the star itself, as opposed to changes one might expect over the pulsation cycle of the star.

Since then, we have investigated its infrared light curve more thoroughly (Appendix A) and have also investigated the question of the apparent 10 μm absorption band in archival data from the SWS on ISO (Appendix D). The SWS data reveal that the 10 μm band can be seen in the spectra of four Galactic carbon stars observed in multiple epochs, and that it generally is strongest when the star is at maximum in its pulsation cycle, which is also the case for WBP 29.

With the completion of the observations of the rest of the sample, we can place WBP 29 in better context. To examine the behavior of the 7.5 μm absorption, we can compare the shift in positions in Figure 6 with the positions of the IRS and MRS epochs on the light curves in Appendix A. We exclude J050629 from consideration due to insufficent phase information. KDM 1691 was observed by the IRS at minimum and by the MRS at maximum, and its 7.5 μm band has weakened. J053441 was observed near minimum by the IRS and near maximum by the MRS, and the 7.5 μm band has weakened in its spectrum also. WBP 17 was observed at maximum by the IRS and at minimum by the MRS, and once again, the observation at minimum has the stronger absorption at 7.5 μm.

In J051803, on the other hand, the 7.5 μm band has grown slightly stronger in the MRS observation, which was closer to maximum, compared to the IRS observation, which was halfway from minimum to maximum. That suggests that the behavior of the 7.5 μm depends on more than just pulsation phase. Similarly, the three reddest Miras present a mixed bag. All three were observed at or near minimum by the IRS and by the MRS at or near maximum. However, the changes in the 7.5 μm band strength are not large, and only two of the three stars (MSX LMC 220 and 774) follow the trend of stronger absorption at minimum. It is possible in these three redder stars that the absorbing layer is much further above the photosphere and does not vary as strongly with the pulsations in the star below it.

To summarize, WBP 29 appears to follow the weak trends of weaker 7.5 μm absorption and stronger apparent 10 μm absorption close to maximum in its pulsation cycle. We conclude that the observed spectral variations most likely result from its pulsations as opposed to evolutionary changes.

5.2. *The impact of the apparent 10 μm absorption band*

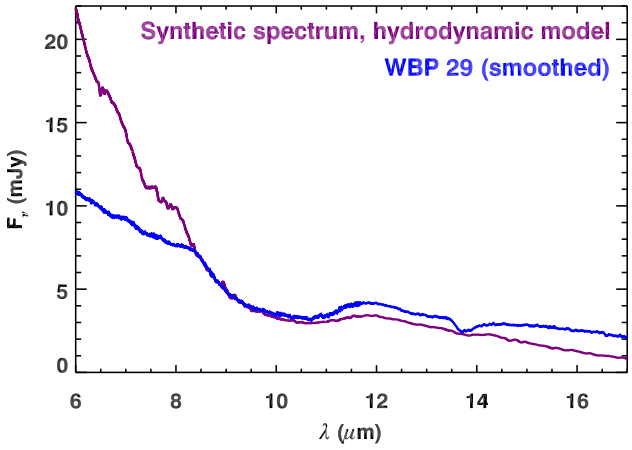

Figure 12. The synthetic spectrum of a hydrodynamic model of a carbon star, computed without dust opacities and scaled to the spectrum of WBP 29. The synthetic spectrum has been downsampled to the MRS wavelength grid and resolution, and the observed spectrum has been smoothed with a 15-pixel boxcar. The model is representative and not fitted specifically to WBP 29. It is for a 1 $M_\odot$ star with $T_{\rm eff}$ = 3000 K and L = 7000 $L_\odot$.

The spectra of the SRVs and the blue Mira WBP 29 in Figures 3 and 4 show a clear depression centered at 10 μm, which could be a molecular absorption band. The depth of this feature and the position of its long-wavelength edge may vary between objects and with time. As Appendix D shows, some Galactic carbon stars observed by the SWS behave similarly.

The carrier of the apparent absorption band at 10 μm is uncertain. We were unable to match the spectral structure in that region closely to any of the molecules considered in the synthetic spectra based on hydrostatic models (viz., C_2H_2, HCN, CS, CO, and C_3). An unidentified molecule not included in our models could be responsible.

Another possibility is that the apparent absorption at 10 μm arises from molecular emission to either side, at 7.5 and 12–15 μm, most likely from C_2H_2, with possible contributions from HCN. These molecules have millions of overlapping transitions in this spectral region, which could produce a raised quasi-continuum in the right conditions. Those conditions could be met if the pulsations in the carbon stars are strong enough to push a layer of gas above the stellar photosphere.

Figure 12 plots a synthetic spectrum from a snapshot of a hydrodynamic model with an extended pulsating atmosphere and a dust-driven wind, alongside a spectrum of WBP 29. This model is based on the DARWIN code (Höfner et al. 2016) and is similar to the carbon-star models by Eriksson et al. (2023) and Siderud et al. (2025), except for the updated molecular opacities as in the hydrostatic COMARCS models (see Section 4.2). While the dynamic simulations include dust, we have computed the synthetic spectrum without dust opacities. That choice makes the synthetic spectrum bluer, but it also removes dust as a possible cause of the apparent absorption at 10 μm. In the synthetic spectrum, the apparent dip at 10 μm is just continuum between molecular emission from other molecules to the red and to the blue. The 7.5 μm band can be seen in emission in Figure 12, as can the broad ν_5 C_2H_2 band with its Q branch at 13.7 μm and the P and R branches extending the band to $\sim$12 and 15 μm.

The similarity of the shape of the synthetic and observed spectra in the 10 μm region demonstrates that the emission scenario is plausible, but direct detailed evidence for emission on either side of the 10 μm feature is lacking. In WBP 29, C_2H_2, HCN, and CS are all detected between 7.0–7.5 μm, but in absorption. The absorption could arise from a cooler layer in the line of sight above the emitting layer. The same argument could also apply at 13.7 μm, where the ν_5 Q branch of C_2H_2 is clearly in absorption.

More work is needed to investigate the nature of this apparent absorption band at 10 μm. Whether it is absorption or continuum between emission regions, its presence is affecting the [6.4]$-$[9.3] color, which is used as a proxy for the ratio of dust to stellar emission and the dust-production rate. In Figure 6, the strong dip in the spectrum of WBP 29 at 10 μm has actually driven the [6.4]$-$[9.3] color negative. We could mitigate by shifting the 9.3 μm band to a shorter wavelength, perhaps $\sim$8.7 μm, which would move it partly out of the 10 μm dip.

Measurements of the SiC dust emission feature are also affected by the 10 μm dip to the blue, as well as absorption from C_2H_2 and other molecules to the red. At first glance,

the synthetic spectrum in Figure 12 might look like it has SiC dust emission at ∼11.3 μm, but it does not. Leisenring et al. (2008) were aware of this challenge and tried to mitigate for it by modeling the "continuum" (from the star, amorphous carbon dust, and molecular absorption) when measuring the flux from SiC dust. A simpler approach would be to focus on the centroid of the extracted feature, as done in Section 4.1. While that might not remove all false positives, it would certainly catch some.

5.3. *MSX LMC 220 and its vanishing dust emission*

The dust emission in the spectrum of MSX LMC 220 has changed dramatically between the IRS and MRS epochs (Figure 5). The IRS spectrum shows a cool dust emission feature that peaks in the vicinity of 18 μm. We examined the spectral images from which the IRS spectrum was extracted and saw no evidence for a contaminating source or anything else unusual, leaving us to conclude that the earlier spectrum really does show this extra dust component. This feature could be related to an 18 μm shoulder seen in the dust emission from some carbon-rich planetary nebulae by Bernard-Salas et al. (2009), who noted that while it was in roughly the right position to be the O–Si–O bending mode in silicate dust, one would expect to see the Si–O stretching mode at 10 μm, which is absent, and oxygen-rich dust would be unlikely in a carbon-rich environment. They were unable to identify the carrier of the feature.

The disappearance of this apparent dust emission in the time between the IRS and MRS epochs is as much of a mystery as its origin in the first place. A simplistic calculation assuming blackbodies for the grains, an outflow velocity of 10 km/s, and $T_{\rm eff}$ = 3000 K for MSX LMC 220 results in changes in dust temperature too small for it to vanish from the infrared spectrum in the intervening 19.6 years. For example, a grain at 150 K when observed by the IRS would have cooled to 140 K by the MRS epoch. A grain temperature as high as 1000 K is highly unlikely, but even then, it would have cooled only to 380 K. MSX LMC 220 is the most luminous source in our sample, which raises the possibility that it is an unusual object and not a normal star on the AGB.

6. SUMMARY

Observations of nine carbon stars in the LMC with the MRS have revealed detailed molecular structure in their spectra. C_2H_2 produces strong and broad absorption bands centered at 7.5 and 13.7 μm that was well-known before. By comparing the observed spectral structure to synthetic spectra from hydrostatic models of carbon stars, we can confidently identify C_3 as the carrier of an absorption band centered at 5.2 μm. The presence of C_3 explains the range of [5.8]−[8.0] colors observed in semi-regular variables. The spectra also show direct evidence of CS at ∼8 μm. The evidence for HCN is indirect, but including it in the fitted mixtures of absorptions from the synthetic spectra in the wavelength intervals with C_2H_2 generally results in lower residuals in the fitting process.

WBP 29 shows spectral structure that looks like a strong and broad 10 μm absorption band in the MRS data that is not apparent in the IRS data. This spectral structure appears in other spectra in our sample. A review of multi-epoch spectroscopy from the SWS on ISO confirms its presence and its variability in Galactic carbon stars. If the apparent 10 μm dip is an absorption band, its carrier is unknown. Hydrodynamic models of carbon stars offer an alternative explanation, that we may be observing a continuum at 10 μm bracketed by emission at shorter and longer wavelengths. The variation appears to be related to the pulsation cycle of the star, with a stronger "dip" at 10 μm when the star is at optical maximum.

This variable spectral structure in the vicinity of the SiC dust emission feature at ∼11.3 μm raises some concern about the reliabilty of measured dust emission strengths using the Manchester Method. That approach fits line segments above absorption bands and below emission features to estimate the continuum, but these spectra have no real continuum in the classic sense. For strong SiC emission, these problems are less significant, but detections of fainter SiC dust features may not be real. They may simply be continuum between absorption bands or shoulders between emission and absorption bands. We recommend that users of the Manchester Method use the measured central wavelengths of bands and features to identify false positives. It may also make sense to shift some of the continuum positions, such as the wavelengths used to measure the [6.4]−[9.3] color, which has served as a proxy for the amount of amorphous carbon dust contributing to the spectrum.

The spectrum of MSX LMC 220 changed significantly between the IRS and MRS epochs, with the older data showing a broad emission feature from apparent dust at ∼18 μm which is not present in the MRS data. The origin of the feature in the previous epoch and the reason for its disappearance are not known.

Support for GCS, KEK, EJM, and RS was provided through grant JWST-GO-03010.005 under NASA contract NAS5-03127. BA and SH acknowledge funding from the European Research Council (ERC) under the European Union's Horizon 2020 research and innovation program (grant agreement No. 883867, project EXWINGS) and the Swedish Research Council (Vetenskapsradet, grant number 2019-04059). JC acknowledges support from the University of Western Ontario and the Natural Sciences and Engineering Research Council of Canada. KJ is supported by the Swedish National Space Agency, and MM is supported by STFC consolidated grant (ST/W000830/1). IM and AAZ acknowledge funding from the OSCARS project, which has received funding from the European Commission's Horizon Europe Research and Innovation programme under grant agreement No. 101129751. RS's contribution to the research described here was carried out at the Jet Propulsion Laboratory, California Institute of Technology, under a contract with NASA.

We gratefully acknowledge the observations of variable stars from the International Database of the American Association of Variable Star Observers (AAVSO) contributed by observers around the world. Some of the observations used here were obtained by the British Astronomical Association for Variable Star Section. This research has made use of the VizieR catalogue access tool at the Strasbourg Astronomical Data center (CDS) in Strasbourg, France (Ochsenbein et al. 2000), the Astrophysics Data System (ADS) funded by NASA under Cooperative Agreement 80NSSC25M7105 at the Smithsonian Astrophysical Observatory. and the Infrared Science Archive (IRSA) operated by IPAC at the California Institute of Technology. It has also utilized data from the Gaia mission of the European Space Agency (ESA) (https://www.cosmos.esa.int/gaia), processed by the Gaia Data Processing and Analysis Consortium (DPAC) and funded by the institutions participating in the Gaia Multilateral Agreement. We also thank the

Coauthor Paola Marigo died while this program was still obtaining observations. Her work strongly contributed to the success of our observing proposal, and we deeply regret that we did not have the opportunity of analyzing and interpreting the spectra alongside her.

Facilities: AAVSO, ISO (SWS), Spitzer (IRAC, IRS), WISE, JWST (MIRI, MRS)

APPENDIX

A. INFRARED LIGHT CURVES

We can use multi-epoch infrared photometry to determine the phase of the pulsational cycle of the stars when the IRS and MRS obtained spectra. We constructed light curves for all nine targets using 3.6 and 4.5 μm photometry from the SAGE and SAGE-Var surveys and 3.4 and 4.6 μm photometry from WISE. Most of the targets have 29 epochs, two from SAGE in 2005, four from SAGE-Var in 2010 and 2011, two from the original WISE mission in 2010, and 21 from the reactivated WISE mission, NEOWISE-R, which ran from 2014 to mid 2024.

The WISE epochs are spaced roughly six months apart. Each of these epochs consists of many individual scans ob-

tained every few hours. Because the LMC is close to the south ecliptic pole, targets in the sample had an average of between 174 and 391 of these individual scans per epoch. The photometry from the individual scans were combined by finding a median, filtering out any data more than 0.35 magnitudes from that value, and then redetermining the median.

The SAGE and SAGE-Var data provide epochs that are not on the six-month cadence of the WISE data, so they can help break degeneracies. The SAGE-Var data were taken contemporaneously with the first two original WISE epochs, which makes them particularly helpful, and the SAGE epochs in 2005 extend the photometric baseline to 19 years.

The IRAC data require a correction to align with the WISE data. The first part of the correction is based on the color corrections generated by Sloan et al. (2016), except that they converted from WISE to IRAC. We repeated their analysis, going in the other direction and adding the WISE epochs since 2016 to the analysis. Table 5 gives the results, based on least-squares fits of lines to the mean magnitudes for all of the carbon stars in the Spitzer/IRS sample defined by Sloan et al. (2016). That sample includes 184 carbon stars in the LMC and 40 in the SMC. Stars with [3.6]−[4.5] colors > 1.55 were excluded because the color corrections for the reddest carbon stars do not appear to follow any coherent trend.

The corrections in Table 5 leave the IRAC data still offset from the WISE data by typically ∼0.15–0.25 mag. These offsets are within the scatter of the photometry for the full sample (see Figure 17 from Sloan et al. 2016), and they are generally unimportant when fitting the large-amplitude variables at the red end of the Mira sequence. For weaker pulsations, though, the offsets make using the IRAC data challenging.

To remove these residual offsets, we first fitted a sinusoid to just the WISE photometry, then used that to determine the mean residuals for the IRAC photometry after the first correction was applied. The second correction to the IRAC photometry then removes these offsets source by source. As explained below for individual stars, two stars show long-term variations in their light curves in addition to the fitted sinusoid, and for those we forced the average residuals for the four SAGE-Var and two original WISE epochs, all taken in 2010–2011, to match.

Our algorithm for fitting light curves is based on the one used by Sloan et al. (2016). We iterated through pulsation periods, typically from 100 to 1,200 days, with a step size of one day, fitted a sine function to the W1 and W2 data independently, and picked the period with the least χ^2 residuals for each. The pulsation periods for W1 and W2 were then averaged and sinusoids fitted to determine the mean magnitudes and amplitudes for W1 and W2. That result served as the basis to determine the second correction to the IRAC photometry.

With the IRAC photometry corrected to be consistent with WISE, we then fitted sinusoids to the combined IRAC and WISE photometry, again iterating from 100 to 1,200 days and searching for the period with the minimum residuals. Table 6 gives the results. The reported period is the average from fitting W1 and W2 separately, and the mean magnitudes and amplitudes were determined by using that mean period. The amplitudes are peak-to-peak for the fitted sinusoid. The uncertainty in period is the standard deviation of the four periods found for W1 and W2 with and without using the IRAC photometry and illustrates how the measured periods depend on the data available. The zero-phase epoch is the average of the results for W1 and W2 in the final fitting step (fixed period, IRAC and WISE data), and the quoted uncertainty is the uncertainty in the mean (i.e., half the difference).

Table 6 gives the periods to nearest day, given the uncertainties of ∼1–5 days. Figures 13 to 15 show the light curves and fitted sinusoids for both unphased and phased data, and Figure 16 plots the residuals from the fitted sinusoids (data−model). The following subsections discuss the results for each star.

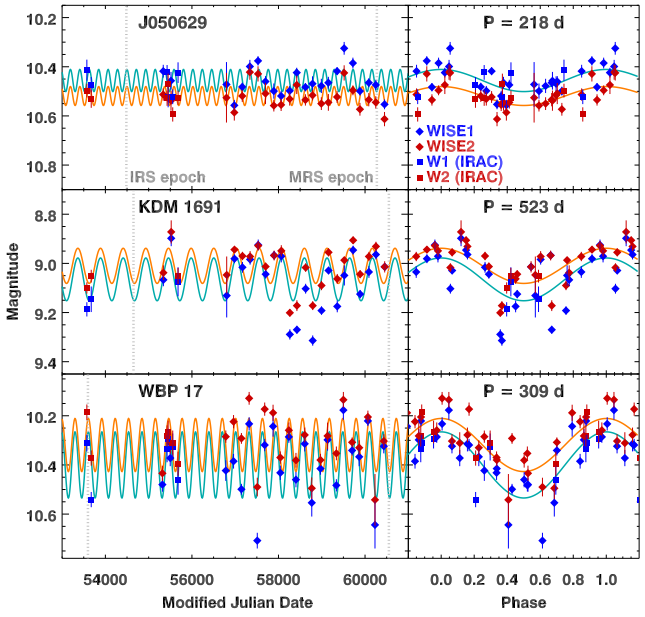

Figure 13. Light curves for the three SRVs in the sample, plotted versus Modified Julian Date (MJD; *left*) and phased (*right*). IRAC data color-corrected to the WISE filters are plotted as squares. The fitted sine functions are plotted in light blue for W1 and orange for W2. In the left-hand panels, the vertical dashed lines give the epochs of the IRS and MRS observations. All three panels have the same vertical range, 0.75 mag.

Table 5. Color and magnitude corrections for carbon stars

Relation	y-intercept	Slope
(W1−W2) − ([3.6]−[4.5]) versus [3.6]−[4.5]	0.1528	0.3003
W1−[3.6] versus [3.6]−[4.5]	0.0352	0.3449
W2−[4.5] versus [3.6]−[4.5]	−0.0224	0.0537

NOTE—These corrections are only valid for [3.6]−[4.5] < 1.55.

Table 6. Fitted light curves

	Period[a]	mean magnitude		amplitude (mag)[a,b]		mean zero-phase	IRAC offsets (mag)[c]	
Target	(d)	W1	W2	W1	W2	MJD	W1	W2
J050629	(218) ± 0.77)	10.456	10.519	0.090	0.077	53845.47 ± 2.97	−0.217	−0.135
KDM 1691	523 ± 1.20	9.065	9.010	0.174	0.143	53364.38 ± 2.93	−0.214	−0.034
WBP 17	309 ± 1.99	10.400	10.319	0.269	0.216	53608.45 ± 0.66	−0.146	−0.072
WBP 29	245 ± 0.81	10.705	10.584	0.367	0.268	53654.67 ± 0.87	−0.179	−0.269
J051803	372 ± 4.74	9.803	9.212	(0.296)	(0.234)	53091.09 ± 6.99	0.013	0.128
J053441[d]	519 ± 2.92	8.970	8.070	0.408	0.391	55439.96 ± 4.65	−0.161	0.015
MSX LMC 220	637 ± 4.47	8.528	7.292	1.131	1.055	53685.42 ± 0.59	0.217	0.266
MSX LMC 774	671 ± 1.67	9.716	8.100	1.312	1.126	53831.45 ± 0.91	−0.138	−0.005
MSX LMC 736	690 ± 1.39	10.740	8.803	1.138	1.120	53472.85 ± 0.58	−0.123	0.005

[a] Values in parentheses are poorly constrained.

[b] Peak-to-peak amplitude of the fitted sinusoid.

[c] Offsets should be subtracted from the IRAC photometry after the first correction.

[d] The results are from the light curve fitted to just the WISE photometry.

A.1. *J050629*

J050629 is classified as an SRV, and it behaves like one, with a small pulsation amplitude and no clear pulsation period, resulting in inconsistent periods in the literature. The OGLE-III survey reported two periods, 741.3 and 154.42 d with similar amplitudes (Soszyński et al. 2009), while the MACHO survey reported periods of 266.52 and 238.49 d, again with similar amplitudes (the survey for Massive Compact Halo Objects, or MACHO; Fraser et al. 2005). Sloan et al. (2024) published a light curve with a period of 154 d, consistent with the shorter OGLE-III period.

The present analysis includes one more WISE epoch than available to Sloan et al. (2024). Adding it and improving the corrections to the IRAC photometry result in two possible pulsation periods, 156 or 218 d. The combined χ^2 residuals for W1 and W2 are smaller for the 218 d period, and that is what is reported here. No one period dominates the light curve of this star. The different published periods may well result from what mode, or resonance between modes, happened to be strongest at the time each survey obtained its data. We can say little about the relative phases of observations for this star, but the pulsation amplitudes are small, so that the star was likely to have been in a similar physical state for both observations.

A.2. *KDM 1691*

KDM 1691 is an SRV, like J050629, but the literature gives a more consistent period somewhere over 500 d, with reported periods of 502.77, 518.7, 529, and 531.95 d, to take some examples from the literature (Soszyński et al. 2009; Fraser et al. 2005; Groenewegen & Sloan 2018; Kim et al. 2014, respectively). However, both the OGLE III and MACHO surveys reported weaker overtone periods of 285.8 and 261.37 d, respectively, indicating that the pulsations are not particularly stable.

Analyzing the WISE data reveals multiple possible periods, at 135, 170, 197, 279, and 522 d, with minimum χ^2

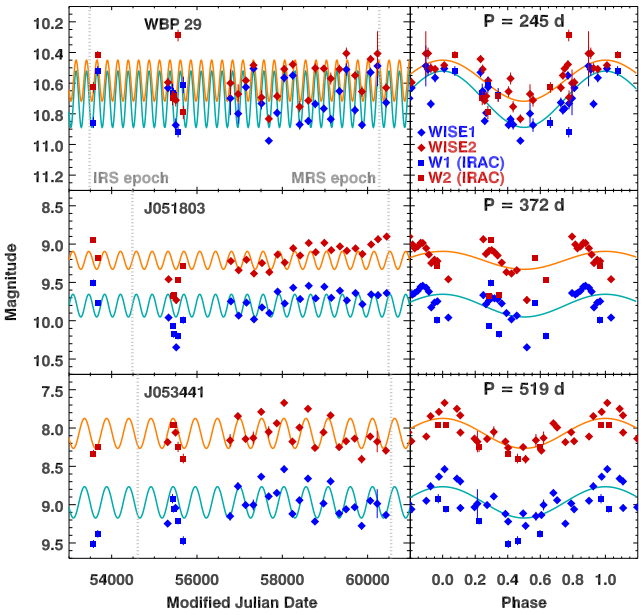

Figure 14. Light curves for the three bluest Miras in the sample. The figure key is the same as Figure 13. The top panel has half the magnitude range as the bottom two (1.2 mag versus 2.4 mag). The nearly one-year period of J51803 and the six-month cadence of the WISE data mean that the fitted pulsation amplitudes are not trustworthy.

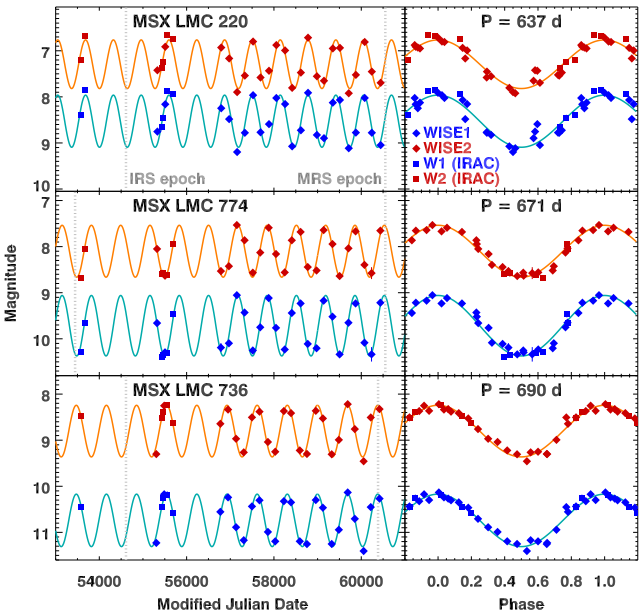

Figure 15. Light curves for the three reddest Miras in the sample. The figure key is the same as Figure 13. All three panels have a vertical extent of 4 mag.

residuals at 197 d for W1 and 522 d for W2. Such complex pulsational behavior should be expected for an SRV. The 522 d period is more consistent with the optical results, and because this star is not reddened by much dust and the optical data have a much better cadence, it is reported here.

The amplitudes of the pulsation cycles in KDM 1691 are twice those of J050729 but they are still less than 0.2 mag, making this star a weak pulsator, despite the apparently long pulsation period. The light curve in Figure 13 and the residuals in Figure 16 show that the pulsation cycle is more complex than a single sinusoid, with a notable excursion to fainter magnitudes between MJD 58000 and 59000 (2017–2020). All of the above is behavior expected for an SRV. Nonetheless, the pulsation period is long enough and characterized well enough that we can state confidently that the star was observed close to its minimum by both the IRS and MRS.

A.3. *WBP 17*

WBP 17 is the third SRV in the sample, and its period is consistently close to 310 d in the literature. The OGLE-III survey reported 314.3 d (Soszyński et al. 2009) and the MACHO survey reported 308.45 d (Fraser et al. 2005). Ou & Ngeow (2022) re-analyzed the OGLE-III data and found a period of 315.44 d. Our analysis suggests that pulsation periods of 244 and 309 d fit the light curves with similar residuals, but the optical data are more finely sampled. Consequently, we report the period closest to ∼310 d.

The pulsation amplitudes of WBP 17 are the strongest of the three SRVs in the sample, but evidence for some irregularities in its behavior can still be seen in its light curve and its residuals at a level of ∼0.2 mag. Despite those deviations from a sinusoid, the light curve is clean enough to show that the IRS observation came close to maximum and the MRS observation close to minimum.

A.4. *WBP 29*

WBP 29 is the least reddened of the six Miras in the sample, and it also has the shortest pulsation period, with OGLE-III reporting 246.7 d (Soszyński et al. 2009) and MACHO reporting 245.82 d (Fraser et al. 2005). Seven other investigators found periods between 240 and 247 d (Ita et al. 2004; Groenewegen 2004; Spano et al. 2011; Kim et al. 2014; Groenewegen & Sloan 2018; Iwanek et al. 2021). Our analysis of the IRAC and WISE data results in a period of 245 d. The fitted light curves imply that the IRS observation was obtained at minimum and the MRS observation at maximum.

A.5. *J051803*

Previous studies indicate a pulsation period for J051803 close to one year. Soszyński et al. (2009) found that the strongest pulsations had a 348.9 d period, Groenewegen & Sloan (2018) reported 352 d, and (Iwanek et al. 2021) reported 362.44 d. A period close to one year is particularly difficult for the WISE cadence, but the IRAC epochs may have broken the degeneracy. For the

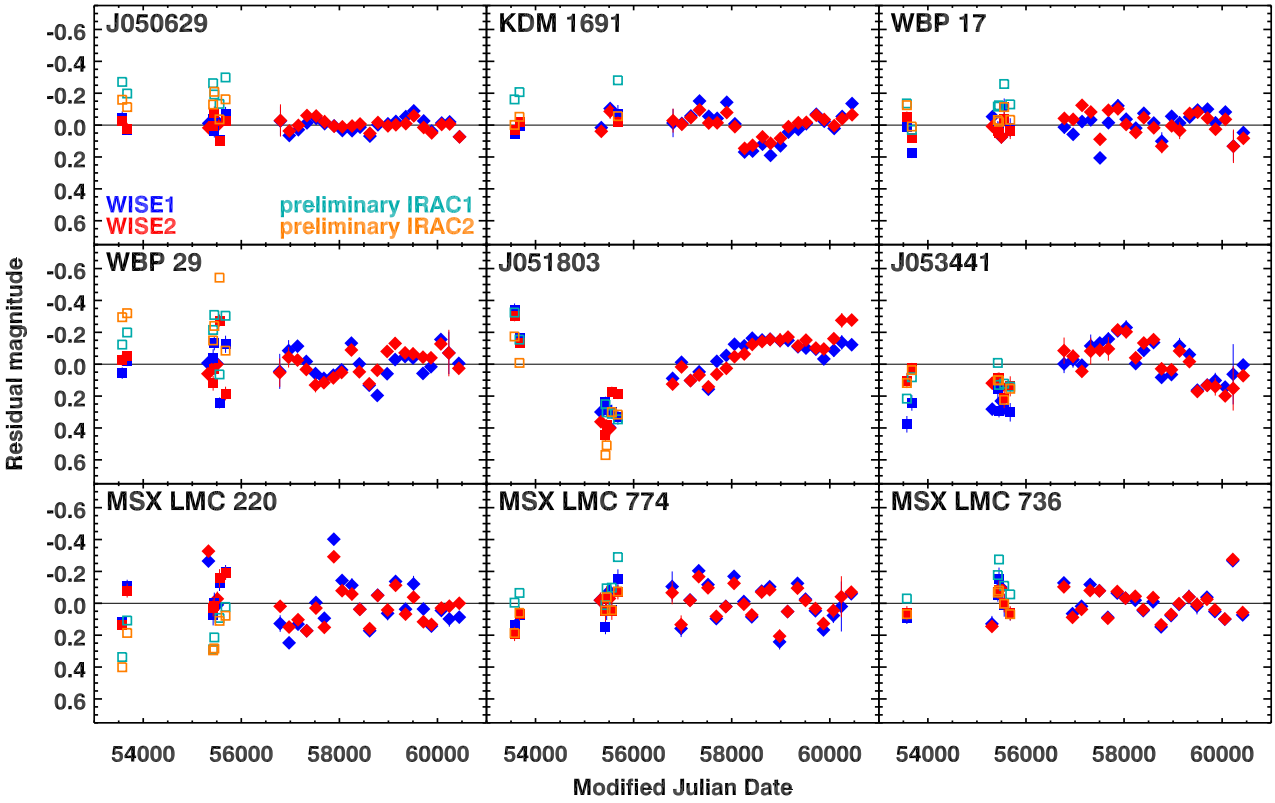

Figure 16. Residuals after subtracting the fitted sinusoids from the observed light curves, with diamonds for WISE observations and squares for color-corrected IRAC data. The IRAC data after the color corrections in Table 5 are plotted as open squares in light blue (for IRAC1) and orange (for IRAC2). The corresponding data after correcting for the residual offsets in Table 6 are plotted as blue or red closed squares.

first pass, instead of using WISE data to find a period, we adopted the period of 362.44 d and used that to determine the corrections for the IRAC photometry.

The light-curve residuals for J051803 in Figure 16 indicate that the star has long-term variations with a peak-to-peak amplitude of ∼0.5 mag. To avoid the impact of this long-term trend, we determined the corrections to the IRAC data using the four SAGE-Var epochs and the two WISE epochs in the interval 55000 < MJD < 56000. Combining the corrected IRAC photometry with WISE gives a pulsation period of 372 d. This pulsation period is still close to a year and the full pulsation cycle is poorly sampled by the IRAC and WISE photometry. For that reason, the pulsation amplitude is poorly constrained, as indicated in Table 6.

The fitted periods for J051803 have been increasing with time, but whether this result is meaningful or not is an open question. The zero-phase epoch for the fitted sinusoids differs by 14 d between W1 and W2, the largest difference for the stars in our sample. That might be a result of a period close to one year, or it could arise from the long-term variations. The residuals show a hint of periodicity, but the available data do not contrain a possible period well. Fitting both the WISE data and the corrected IRAC data yields a period of ∼6140 d in W1 and ∼7130 d in W2, which is a rather significant difference of ∼15%. While the period may not be well contrained, the peak-to-peak amplitude of a sinusoid fitted to these residuals is significant, 0.93 mag in W1 and 1.0 mag in W2. These long-period results should be viewed more as a suggestion than a meaningful measurement. With all of these uncertainties, the only safe conclusion is that J051803 has a complex light curve.

The fitted light curve for J051803 suggests that the IRS epoch was obtained as the source was climbing from minimum to maximum and the MRS epoch was close to maximum. But all the caveats for the light curve for this source should be kept in mind.

A.6. *J053441*

J053441 has a light curve similar to J051803, except that the primary pulsation period is considerably longer than one year. Previous investigations found periods between 489 d and 548 d (Soszyński et al. 2009; Spano et al. 2011; Groenewegen et al. 2020; Iwanek et al. 2021; Ou & Ngeow 2022). Our analysis of the WISE photometry results in a period of 519 d. As with J051803, the light curve shows long-term variations (see Figure 16), forcing us to determine a correction for the IRAC data using just the data with 55000 < MJD < 56000. Despite those corrections, adding the IRAC data did not help us determine a primary period, because the curve-fitting software failed to converge at the minimum χ^2

residuals in W2. The period in W1 was 522 d, and in W2 at least 523 d. Table 6 gives the results for just the WISE data, although the uncertainty in the period reflects the range in the fitted period introduced by adding the IRAC data.

J053441, like J051803, shows possible periodicity in its residuals. Fitting both the WISE data and the corrected IRAC data give periods of ∼7700 d for W1 and ∼5700 d for W2, but the discrepancy between the two filters is even larger than for J051803. The peak-to-peak amplitudes are smaller, 0.90 mag in W1 and 0.57 mag in W2. The long-term variations are clear enough, but the available data do not allow them to be properly quantified.

A.7. *MSX LMC 220*

For MSX LMC 220, we find a period of 644 d with just the WISE data. Adding the corrected IRAC data shifts this result to 637 d. Previous results have similar periods of 625 and 632 d (Groenewegen et al. 2009; Groenewegen & Sloan 2018), although OGLE-III reported periods of 313 and 1805 d (Soszyński et al. 2009). The light curves based on the IRAC and WISE data indicate fairly steady pulsations over the past 20 years in the 3–5 μm range (Figure 14), but the residuals in Figure 16 show deviations up to ∼0.4 mag in some isolated epochs, suggesting that the pulsations are not completely settled. The pulsation cycle is long enough and the pulsations steady enough to conclude with some confidence that the IRS epoch came close to minimum, while the MRS epoch came as MSX LMC 220 was roughly halfway to maximum.

A.8. *MSX LMC 774*

Moving to the red end of the Mira sequence leads to steadier and stronger pulsations, and MSX LMC 774 follows that trend. Its dust shell effectively erases the star from the optical skies, so it does not appear in the OGLE-III and MACHO surveys. Using the IRAC data and the limited number of WISE epochs available at the time, Sloan et al. (2016) found a period of 670 d, and with more epochs and a slightly different technique, Groenewegen (2022) found periods of 680 d in W1 and 678 d in W2. Using even more WISE epochs, we find a period of 668 d. The well-behaved pulsation cycle and long period of MSX LMC 774 constrain the epochs of the IRS and MRS spectroscopy well, with the IRS observing the star just before minimum and the MRS very close to maximum.

A.9. *MSX LMC 736*

MSX LMC 736 is another Mira too reddened by its own dust to appear in optical variability surveys. Previous measurements of its period have been based on the six SAGE and SAGE-Var epochs and increasing numbers of epochs from WISE: 686, 683, 672, and 690 d (Sloan et al. 2016; Groenewegen & Sloan 2018; Groenewegen et al. 2020; Sloan et al. 2024, respectively). This work duplicates the last period, 690 d, even though it adds one WISE epoch and corrects the IRAC photometry for residuals. As with MSX LMC 774, the light curve constrains the IRS and MRS epochs well, with the first just after minimum and the second right at maximum.

B. LUMINOSITIES

Table 7 presents bolometric luminosities for the stars in our sample, determined using two methods and compared to the results from Groenewegen & Sloan (2018). Our first method is to apply the PySSED software (ver. 1.1), which constructs a spectral energy distribution (SED) for a source from an automated look-up of the available photometry in VizieR and integrates the result through wavelength space (McDonald et al. 2024, 2025). Our second method of determining the bolometric luminosity uses a curated set of photometry and the spectra from the IRS and MRS.

For the second (curated) method, the mid-infrared photometric data were limited to the mean 24 μm photometry from the SAGE survey (Meixner et al. 2006) and the mean results in the WISE filters at 3.4 and 4.6 μm reported in Appendix A (including the color-corrected IRAC photometry from SAGE and SAGE-Var). We also used near-infrared photometry from the Two-Micron All-Sky Survey (2MASS; Skrutskie et al. 2006), 2MASS 6X (same reference), photometry from the Infrared Spectral Survey (IRSF; Kato et al. 2007), the Deep Near Infrared Survey of the Southern Sky (DENIS; Cioni et al. 2000), and the Vista Magellanic Cloud survey (VMC Data Release 6; Cioni et al. 2011). Photometry at shorter wavelengths came from the OGLE III survey (Soszyński et al. 2009), the MACHO survey (Fraser et al. 2008), the Magellanic Clouds Photometric Survey (MCPS; Zaritsky et al. 2004), the SkyMapper Southern Sky Survey (Data Release 4; Onken et al. 2024), and Gaia (Data Release 3; Gaia Collaboration 2023). We did not include the K_s photometry from the VMC because it gave the faintest magnitude at K_s in five of the nine sources. We omitted the MACHO R_c magnitudes because they were low outliers in all four sources for which data were available. We also omitted the MCPS i-band data for J053441 and MSX LMC 220 because they were outliers and one of the DENIS I-band magnitudes for MSX LMC 220 for the same reason. For both J051803 and MSX LMC 736, some care was required to avoid neighboring sources. We averaged the remaining data at I (0.77–0.80 /um), J (1.22–1.25 μm), H (1.61–1.67 μm), and K_s (2.23–2.16 μm).

We combined the MRS and IRS data by regridding the MRS to the IRS, truncating the MRS beyond 20 μm, averag-

Table 7. Bolometric luminosities and magnitudes

	Bolometric luminosity ($L_\odot$)				
Target	Groenewegen & Sloan (2018)[a]	PySSED method	Curated SED and spectra	mean[b]	M_{bol} (mag)
J050629	(3489)	3818	3824	3821 ± 3	−4.21 ± 0.00
KDM 1691	12707	13595	14653	13652 ± 562	−5.59 ± 0.04
WBP 17	(7268)	5201	5824	5513 ± 312	−4.60 ± 0.06
WBP 29	5032	5084	4910	5009 ± 52	−4.50 ± 0.01
J051803	(4851)	2968	3570	3269 ± 301	−4.04 ± 0.10
J053441	8198	10232	9145	9192 ± 588	−5.16 ± 0.07
MSX LMC 220	(23388)	16290	15230	15760 ± 530	−5.74 ± 0.04
MSX LMC 774	7574	7342	9620	8179 ± 723	−5.03 ± 0.10
MSX LMC 736	9311	7168	8150	8210 ± 619	−5.04 ± 0.08

[a] Values not used in mean luminosity are in parentheses.

[b] Uncertainties are the uncertainty in the mean.

ing the spectra where they overlapped, and normalizing the remaining spectral data to align with the average. To normalize the resulting spectra to the approximate mean of the light curve, we used the phase information for the epochs in Appendix A. For six of the nine carbon stars, we forced the combined spectrum to the average of the two. The exceptions were KDM 1691 and MSX LMC 220, where we forced the IRS to align with the MRS, and J051803, where we did the opposite. Figure 17 shows the resulting SEDs for all nine sources, along with the spectra from the MRS and IRS.

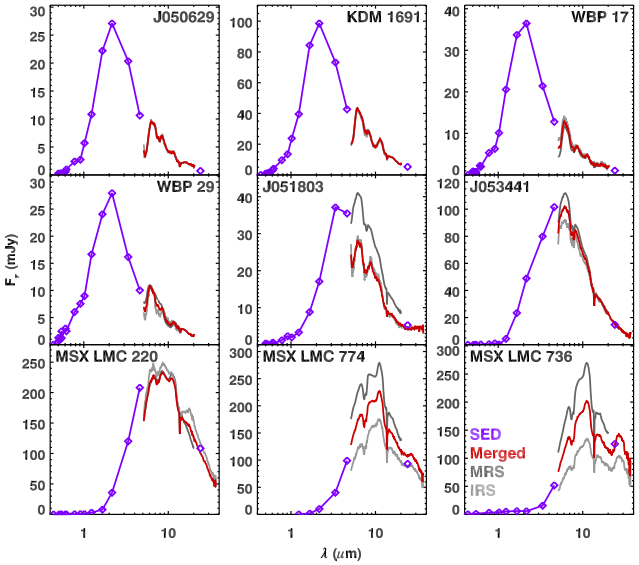

Figure 17. Spectral energy distributions and merged spectra from the MRS and IRS for the nine stars in the sample. The plotted data are not corrected for interstellar aborption.

The PySSED code uses Gaia-based extinction maps from Lallement et al. (2022). Groenewegen & Sloan (2018) assumed A_v = 0.15 in the LMC, and we followed their lead. We used the interstellar extinction from Rieke & Lebofsky (1985) to 1.35 μm and Chiar & Tielens (2006) past 1.35 μm. The extinction affected the results by ∼3% for the bluer sources and ∼1–2% for the redder sources, which means that the specific choice for the extinction correction has little effect.

We integrated the combination of SED and spectra to determine the bolometric luminosity of each source, using a Wien tail for a 3000 K blackbody to extrapolate to the blue from the shortest observed wavelength and a Rayleigh-Jeans tail to extrapolate from the longest observed wavelength to the red. For the three SRVs and WBP 29, the usable spectral data only extended as far as 20 μm, so we included the MIPS 24 μm photometry in the SED. For the remaining five Miras, the spectral data extended to 38 μm and we omitted the MIPS photometry.

For the luminosities and bolometric magnitudes, we assumed a distance modulus to the LMC of 18.48 mag (Pietrzyński et al. 2019). We shifted the results from Groenewegen & Sloan (2018) to this distance; they assumed a distance of 50.0 kpc ($m - M$ = 18.495 mag).

As Table 7 shows, the PySSED method generally obtained similar results to the combination of curated SEDs and MRS and IRS spectra, in no small part because both methods shared much of the same photometry. Given the work involved in curating the photometry, the similar results are a strong argument for using the more automated PySSED method. Groenewegen & Sloan (2018) used the photome-

try available at that time to construct a model of the star and from that determined the bolometric luminosity. That method produced results which differed more significantly. We excluded the model-based luminosities when they doubled the standard deviation estimated from our two methods (Table 7 shows the excluded values in parentheses). The remaining five luminosities were averaged with the results from our two methods to provide the mean luminosities in Table 7 (and Table 1).

C. FITTING THE BAND STRUCTURE IN THE SPECTRA

Figures 18 to 25 compare the flattened spectra of the carbon stars in our sample to the best-fitting combination of absorbing molecules, using synthetic spectra generated from a 2800 K model for the SRVs and 3100 K for the Mira variables. The plotted spectra cover the eight wavelength intervals defined in Section 4.2. The observed spectra are corrected for the radial velocities determined in Section 4.2.1 and listed in Table 3.

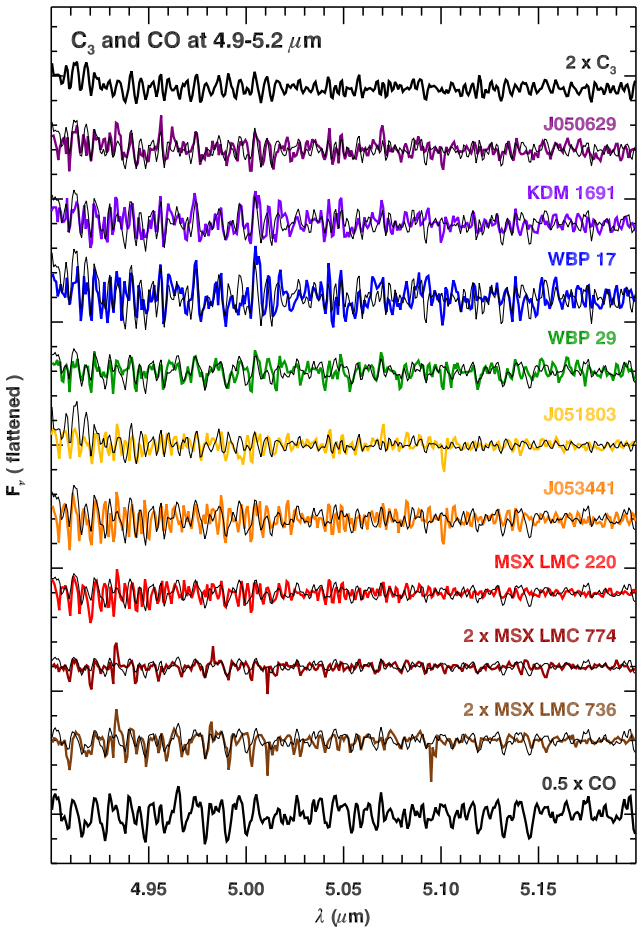

Figure 18. The flattened spectra at 4.9–5.2 μm for the nine carbon stars in the sample (in color) and the best-fitted combination of molecular spectra for each (black). The C_3 spectrum at the top is from the synthetic spectrum based on an effective temperature of 3100 K. The CO spectrum at the bottom is for 2800 K. Both are for a C/O ratio of 2.0. The observed spectra are shifted to correct for the radial velocities in Table 3.

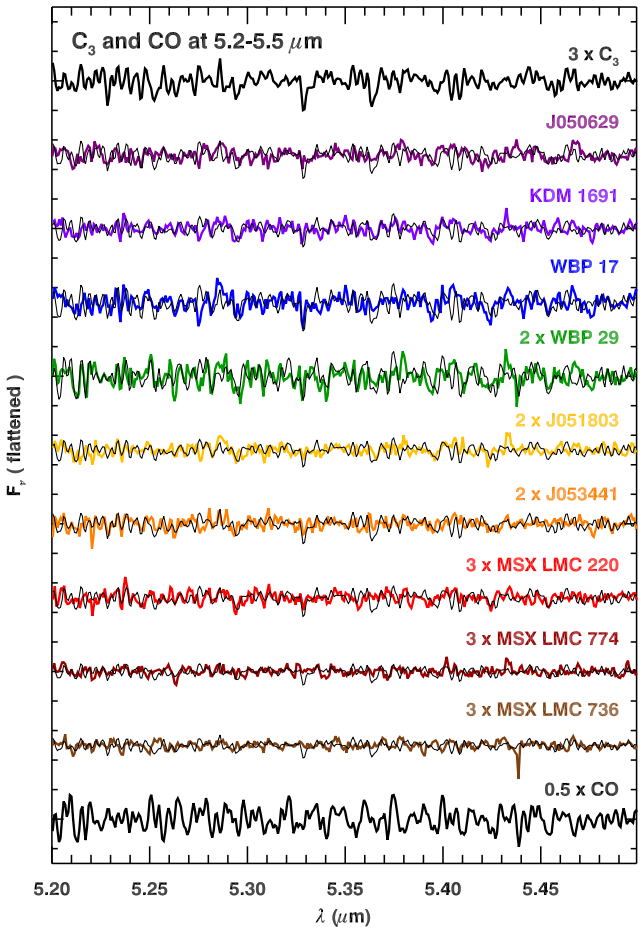

Figure 19. As Figure 18, but for 5.2–5.5 μm.

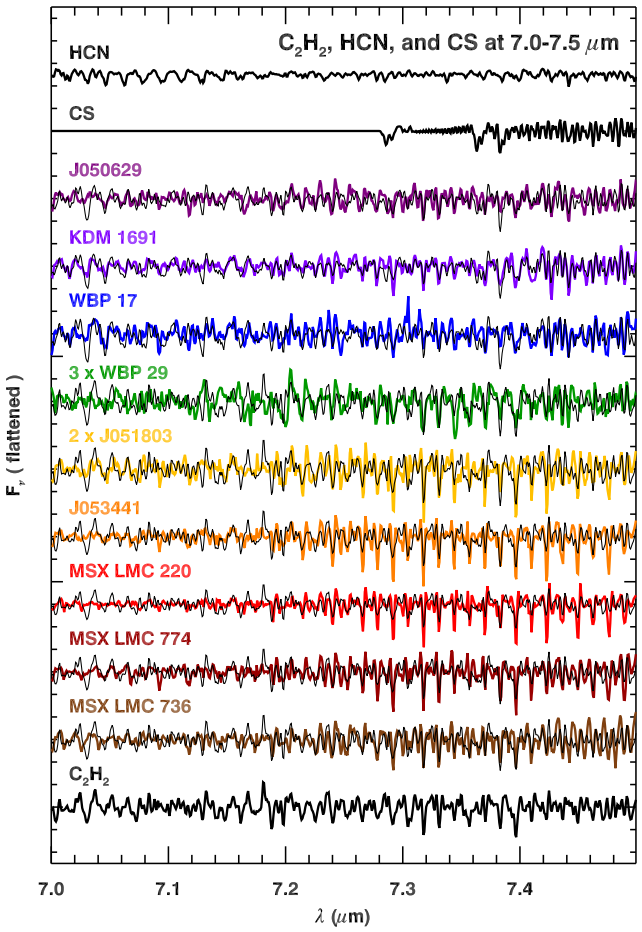

Figure 20. The flattened spectra at 7.0–7.5 μm, with the observed spectra in color and the fitted molecular spectra in black. The HCN and CS at the top are from the synthetic spectra with $T_{\rm eff}$ = 3100 K, and the C_2H_2 at the bottom is from the 2800 K spectrum. Both have a C/O ratio of 2.0. The observed spectra are corrected for the radial velocities in Table 3.

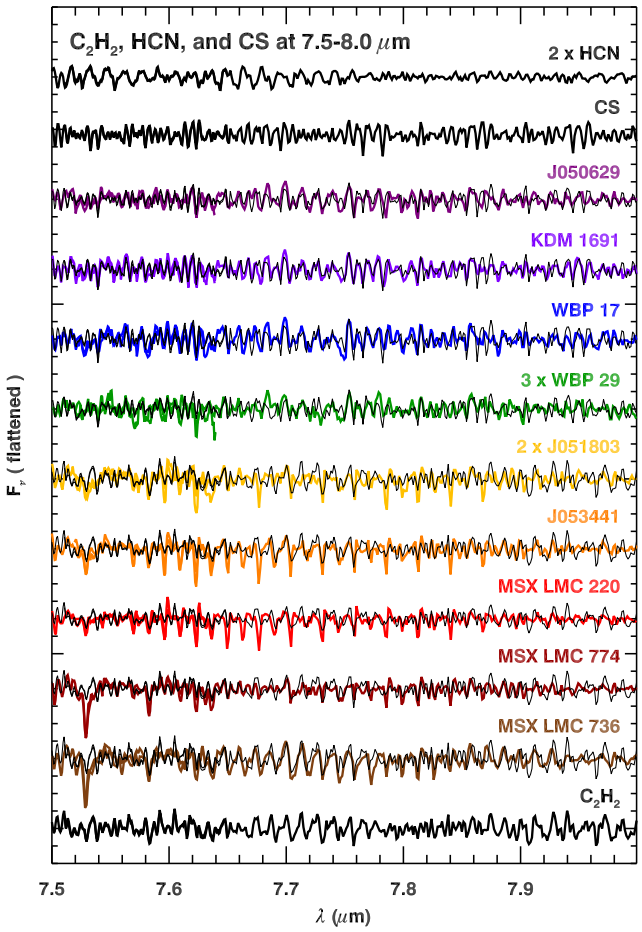

Figure 21. As Figure 20, except for 7.5–8.0 μm.

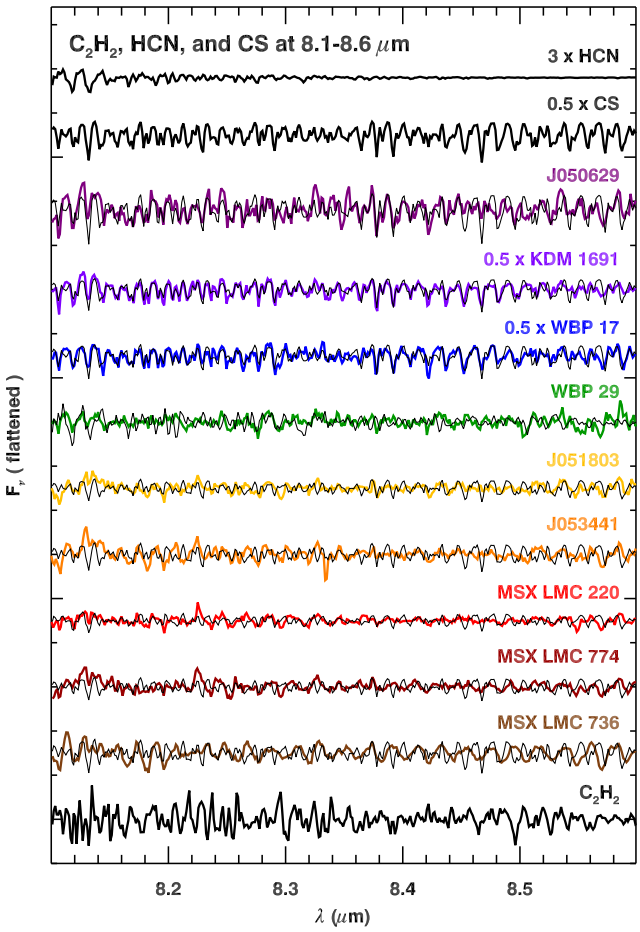

Figure 22. As Figure 20, but for the interval 8.1–8.6 μm.

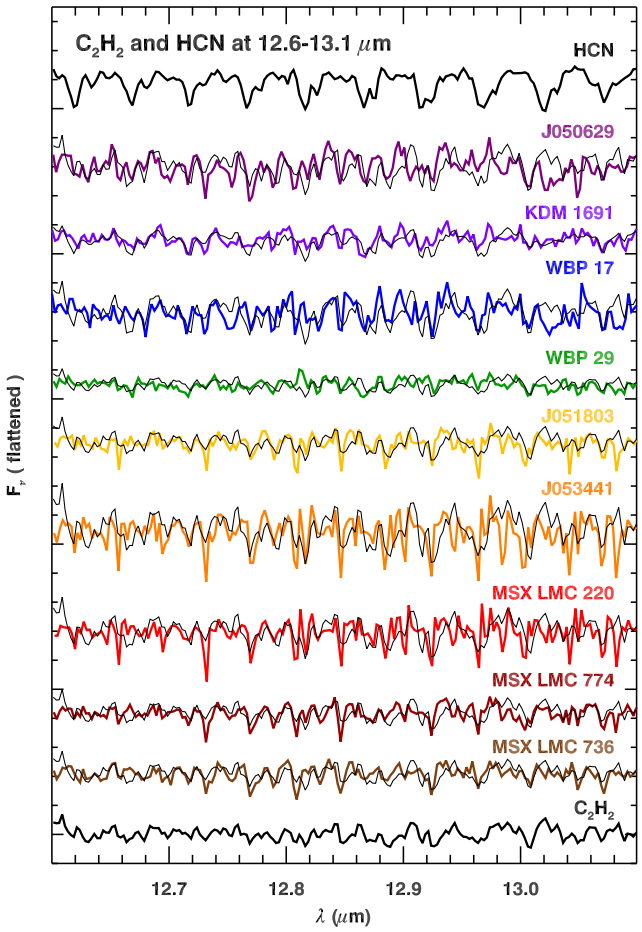

Figure 23. The flattened observed spectra at 12.6–13.1 μm (in color) compared to fitted molecular spectra (black). The HCN spectrum at the top is for $T_{\rm eff}$ = 3100 K and a C/O ratio = 2.0. The C_2H_2 at the bottom is for 2800 K and the same C/O ratio. The observed spectra are corrected for the radial velocities in Table 3.

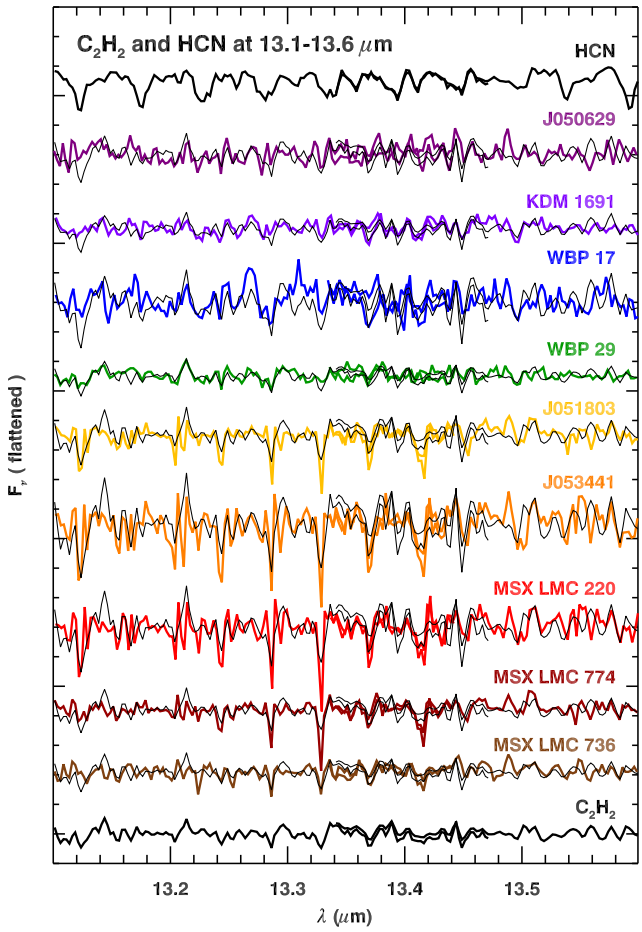

Figure 24. As Figure 23, but for 13.1–13.6 μm.

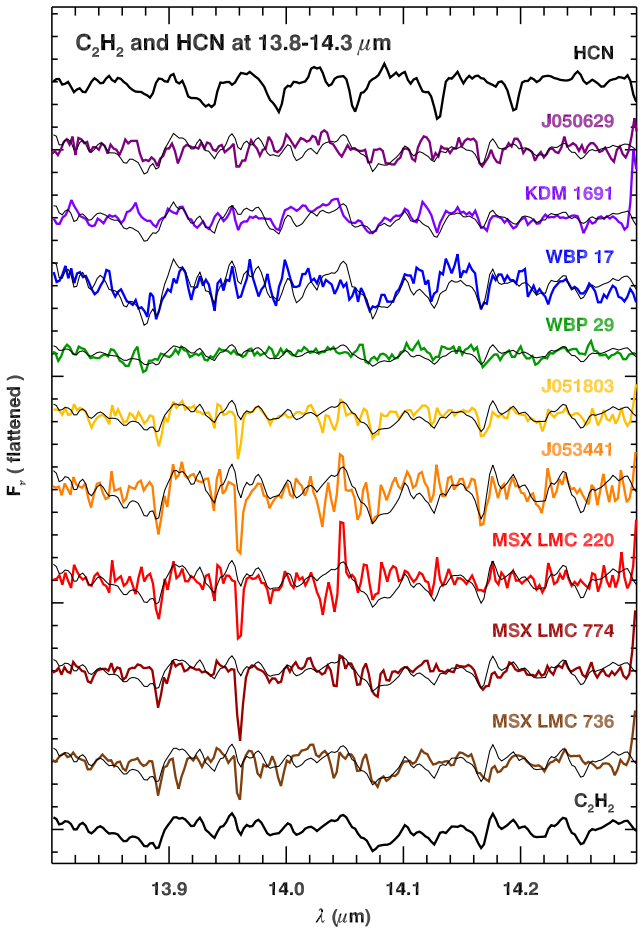

Figure 25. As Figure 23, but for 13.8–14.3 μm.

D. MULTI-EPOCH SPECTRA FROM THE INFRARED SPACE OBSERVATORY

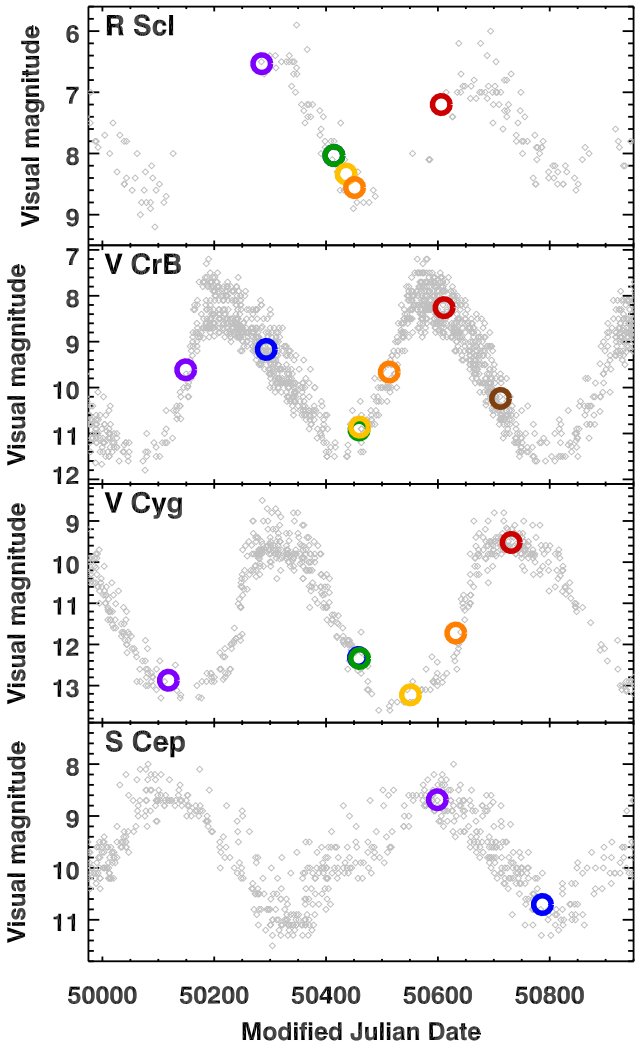

Figure 26. Light curves from the AAVSO in grey with the epochs of the SWS observations plotted in color. The magnitudes at the SWS epochs are estimated from AAVSO observations with ±20 d. In the panels for R Scl and V Cyg, the second and third spectra were obtained the same day, so the green plotting symbol completely covers the blue. Figure 27 plots the spectra in the same colors.

The SWS on ISO obtained reliable infrared spectra of 42 Galactic carbon stars (Leisenring et al. 2008; Sloan et al. 2016). Several of these stars were observed multiple times, and we examined the individual spectra of all of them for variations in the apparent 10 μm absorption band, using the spectra processed by Sloan et al. (2003). Four sources showed this apparent absorption, and it varied in each of them.

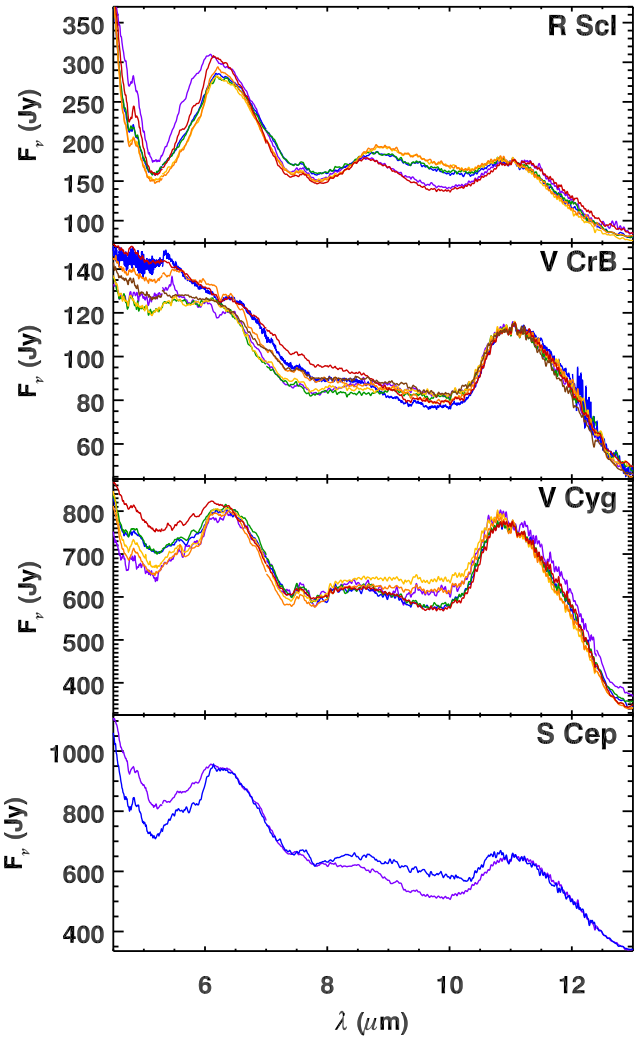

Figure 27. Spectra from each SWS observation for the four Galactic carbon stars chosen to compare the behavior of the 10 μm absorption band. The spectra are plotted with the same colors in Figure 26. All spectra are normalized to the first spectrum at 11.0–11.2 μm.

Table 8 provides basic information about the four Galactic carbon stars, including their [6.4]−[9.3] colors, which range from ∼0.3 to ∼0.5. That interval includes the MRS targets J051803 and J053441. R Scl is an SRb variable, and the other three are Miras. The pulsation periods range from ∼360 to 480 d, again similar to J051803 and J053441.

Table 9 gives the details of each SWS observation considered. Two observations of R Scl and V CrB occurred on the same day; we treated these independently, but they corraborate each other well.

To check the spectral variations with the pulsation phase, we analyzed visual photometry of the four Galactic carbon stars from the American Association of Variable Star Observers (AAVSO; Kloppenorg 2025). We excluded upper limits and data described as "discrepant." Figure 26 plots the AAVSO light curves, and it also shows when the SWS data

Table 8. Comparison carbon stars in the Galaxy

Target	RA (J2000)[a]	Decl. (J2000)[a]	Spec. Type	Spec. Ref.[b]	Variability[c] Type	Period (d)	[6.4]−[9.3] (mag)[d]
R Scl	21.783725	−32.801921	C6.4p	S44	SRb	370	0.27
V CrB	237.380467	+39.571637	C6,2e	S44	Mira	357.63	0.40
V Cyg	310.326115	+48.141336	C5,3e	Y75	Mira	421.27	0.52
S Cep	323.803430	+78.624496	C6.3e	Y75	Mira	484.4	0.30

[a] From Gaia EDR3 (Gaia Collaboration 2021).

[b] S44 = Sanford (1944); Y75 = Yamashita (1975).

[c] Samus et al. (2017).

[d] Leisenring et al. (2008).

Table 9. SWS observing log

Target	TDT[a]	Obs. date (MJD)
R Scl	24701012	50285
	37801213	50414
	37801443	50414
	39901911	50436
	41401514	50451
	56900115	50606
V CrB	11105149	50149
	25502252	50293
	42200213	50459
	42300201	50460
	47600302	50513
	57401003	50611
	67600104	50712
V Cyg	08001855	50118
	42100111	50458
	42300307	50460
	51401308	50551
	59501909	50632
	69500110	50731
S Cep	56200926	50599
	75100424	50787

[a] Time Designated Target number. The first three digits give the approximate number of days since the launch of ISO.

were obtained. For each SWS epoch, we estimated a visual magnitude by averaging the AAVSO data within an interval of ±20 d. While S Cep has only two epochs, compared to 6–7 epochs each for the other three stars, they fall conveniently close to a visual maximum and minimum.

Figure 27 plots the individual spectral observations from the SWS. The first and last observations of R Scl, both taken at or close to maximum, show stronger apparent absorption at 10 μm than the four observations taken as the star approached minimum. The correlation of the strength of the band with phase is strong, with the two observations closest to minimum showing the weakest apparent absorption. S Cep shows the same dependency of apparent 10 μm absorption with phase, with the caveat that we only have two epochs.

If we had the same two observations of V Cyg, we could expect to draw a similar conclusion, with the last epoch coming at maximum and showing deep apparent 10 μm absorption and the fourth epoch (gold) coming at minimum and showing the weakest apparent absorption. The remaining epochs, however, do not follow such a consistent pattern, with the second and third epochs (blue and green) obtained as the star approached mininum and showing almost as much apparent absorption as when the star was at maximum. V CrB also shows complex behavior. While the epochs closest to minimum are among the spectra with the weakest apparent absorption (green, gold, and brown), and the epoch closest to maximum among the strongest (red), the epochs at intermediate phases do not appear to follow a coherent pattern.

We conclude that the SWS data confirm the presence of a varying apparent absorption component at 10 μm in the spectra of carbon stars observed with the MRS, and that the trend is generally for stronger apparent absorption when the central star is at its maximum in the optical.

REFERENCES

Allamandola, L. J., Tielens, A. G. G. M., & Barker, J. R. 1989, ApJS, 71, 733

Aoki, W., Tsuji, T., & Ohnaka, K. 1998, A&A, 340, 222

Aoki, W., Tsuji, T., & Ohnaka, K. 1999, A&A, 350, 945

Aringer, B., Girardi, L., Nowotny, W., et al. 2016, MNRAS, 457, 3611

Aringer, B., Marigo, P., Nowotny, W., et al. 2019, MNRAS, 487, 2133

Barber, R. J., Strange, J. K., Hill, C., et al. 2014, MNRAS, 437, 1828

Bernard-Salas, J., Peeters, E., Sloan, G. C., et al. 2009, /apj, 699, 1541

Bladh, S., Eriksson, K., Marigo, P., et al. 2019, A&A, 623, L119

Boyer, M. L., Srinivasan, S., Riebel, D., et al. 2012, ApJ, 748, 40

Blanco, B. M., Blanco, V. M., & McCarthy, M. F. 1978, Nature, 271, 638

Blanco, V. M., McCarthy, M. F., & Blanco, B. M. 1980, ApJ, 242, 938

Chiar, J. E., & Tielens, A. G. G. M. 2006, ApJ, 637, 774

Cherchneff, I. 2006, A&A, 456, 1001

Choudhury, S., Subramaniam, A., & Cole, A. A. 2016, MNRAS, 455, 1855

Chubb, K. L, Tennyson, J., & Yurchenko, S. N. 2020, MNRAS, 493, 1531

Cioni, M.-R. L., Clementini, G., Girardi, L., et al. 2011, A&A, 527, 116

Cioni, M.-R. L., & Habing, H. J. 2003, A&A, 402, 133

Ciono, M.-R. L., Loup, C., Habing, H. J., et al. A&AS, 114, 235

de Graauw, Th., Haser, L. N., Beintema, D. A., et al. 1996, A&A, 315, L49

Eriksson, K., Höfner, S., & Aringer, B. 2023, A&A, 673, 21

Fazio, G. G., Hora, J. L., Allen, L. E., et al. 2004, ApJS, 154, 10

Feast, M. W. 2013, in Planets, Stars, and Stellar Systems Vol. 5, T. D. Oswalt & G. Gilmore (Dordrecht: Springer), 829

Fraser, O. J., Hawley, S. L, & Cook, K. H. 2008, AJ, 136, 1242

Fraser, O. J., Hawley, S. L, Cook, K. H., & Keller, S. C. 2005, AJ, 129, 768

Frenklach, M., & Feigelson, E. D. 1989, ApJ, 341, 372

Gaia Collaboration, Prusti, T., de Bruijne J. H. H., et al 2016, A&A, 595, 1

Gaia Collaboration, Brown, A. G. A., Vallenari, A., et al. 2021, A&A, 649, 1

Gaia Collaboration, Vallenari, A., Brown, A. G. A., et al. 2023, A&A, 674, 1

Gardner, J. P., Mather, J. C., Abbot, R., et al. 2023, PASP, 135, 68001

Groenewegen, M. A. T. 2004, A&A, 425, 595

Groenewegen, M. A. T. 2004, A&A, 659, 145

Groenewegen, M. A. T., Nanni, A., Cioni, M.-R. L., et al. 2020, A&A, 636, 48

Groenewegen, M. A. T., Sloan, G. C., Soszyński, I., & Petersen, E. A. 2007, A&A, 506, 1277

Groenewegen, M. A. T., & Sloan, G. C. 2018, A&A, 609, 114

Groenewegen, M. A. T., Wood, P. R., & Sloan, G. C. 2007, MNRAS, 376, 313

Habing, H. J. 1996, A&A Rv, 7, 97

Harris, G. J., Larner, F. C., Tennyson, J., et al. 2008, MNRAS, 390, 143

Höfner, S., Bladh, S., Aringer, B., & Ahuja, R. 2016, A&A, 594, 108

Höfner, S. & Olofsson, H. 2018, A&A Rv, 26, 1

Houck, J. R., Roellig, T. L., & van Cleve, J., et al. 2004, ApJS, 154, 18

Ita, Y., Tanabé, T., Matsunaga, N., et al. 2004, MNRAS, 353, 705

Iwanek, P., Soszyński, I., & Kozłowski, S. 2021, ApJ, 919, 99

Kato, D., Nagashima, C., Nagayama, T., et al. 2007, PASJ, 59, 615

Kessler, M., Anderegg, M. E., Clavel, J., et al. 1996, A&A, 315, L27

Kessler, M., Müller, T. G., Leech, K., et al. 2003, The ISO Handbook, Vol. I: ISO—Mission & Satellite Overview (ESA SP-1262)

Kim, D.-W., Protopapas, P., Bailer-Jones, C. A. L., et al. 2014, A&A, 566, 43

Kloppenborg, B. K. 2025, Observations from the AAVSO International Database (https://www.aavso.org)

Kraemer, K. E., Sloan, G. C., Keller, L. D., et al. 2019, ApJ, 887, 82

Lallement, R., Vergely, J. L., Babusiaux, C., & Cos, N. L. J. 2022, A&A, 661, 147

Law, D. R., Argyriou, I., Gordon, K. D., et al. 2024, AJ, in press (arXiv 2409.15435)

Leech, K., Kester, D., Shipman, R., et al. 2003, The ISO Handbook, Vol. V: SWS—The Short Wavelength Spectrometer (ESA SP-1262)

Leisenring, J., Kemper, F., & Sloan, G. C. 2008, ApJ, 681, 1557

Li, G., Gordon, I. E., Rothman, L. S., et al. 2015, ApJS, 216, 15

Liljegren, S., Höfner, S., Nowotny, W., & Eriksson, K. 2016, A&A, 589, 130

Lynas-Gray, A. E., Polyansky, L., Tennyson, J., et al. 2024, MNRAS, 535, 1439

Mainzer, A., Bauer, J., Cutri, R. M., et al. 2014, ApJ, 792, 30

Martin, P. G., & Rogers, C. 1987, ApJ, 322, 374

Matsuura, M., Barlow, M. J., Zijlstra, A. A. et al. 2009, MNRAS, 396, 918

Matsuura, M., Wood, P. R., Sloan, G. C., et al. 2006, MNRAS, 371, 415

Matsuura, M., Woods, P. M., & Owen, P. J. 2013, MNRAS, 429, 2527

Mattsson, L., Wahlin, R., Höfner, S., et al. 2008, A&A, 484, L5

Mattsson, L., Wahlin, R., & Höfner, S. 2010, A&A, 509, 14

McDonald, I., Srinivasan, S., Scicluna, P., et al. 2025, MNRAS, 541, 516

McDonald, I., & Trabuchhi, M. 2019, MNRAS, 484, 4678

McDonald, I., Zijlstra, A. A., Cox, N. L. J., et al. 2024, RASTI, 3, 89

Meixner, M., Gordon, K. D., Indebetouw, R., et al. 2006, AJ, 132, 2268

Onken, C. A., Wolf, C., Bessell, M. S., et al. 2024, PASA, 41, 61

Ou, J.-Y., & Ngeow, C.-C. 2022, AJ, 163, 192

Ochsenbein, F., et al. 2000, "The VizieR database of astronomical catalogues," DOI: 10.26093/cds/vizier

Paulose, G., Barton, E. J., Yurchenko, S. N., & Tennyson, J. 2015, MNRAS, 454, 1931

Piatti, A. E., & Geisler, D. 2013, AJ, 145, 17

Pietrzyński, G., Graczyk, D., Gallenne , A., et al. 2019, Nature, 567, 200

Pontoppidan, K. M., Salyk, C., Banzatti, A., et al. 2024, ApJ, 963, 158

Renzini, A., & Voli, M. 1981, A&A, 94, 175

Riebel, D., Boyer, M. L., Srinivasan, S., et al. 2015, ApJ, 807, 1

Rieke, G. H., & Lebofsky, M. H. 1985, ApJ, 288, 618

Salpeter, E. E. 1952, ApJ, 115, 326

Samus, N. N., Kazarovets, E. V., Durlevich, O. V., et al. 2017, General Catalogue of Variable Stars: Version GCVS 5:1

Sanford, R. F. 1944, ApJ, 99, 145

Siderud, E., Eriksson, K., Höfner, S., & Bladh, S. 2025, A&A, 697, 52

Skrutskie, M. F., Cutri, R. M., Stiening, R., et al. 2006, AJ, 131, 1163

Sloan, G. C., Kraemer, K. E., Aringer, B., et al. 2024, Galaxies, 12, 61

Sloan, G. C., Kraemer, K. E., Price, S. D., & Shipman, R. F. 2003, ApJS, 147, 379

Sloan, G. C., Kraemer, K. E., Wood, P. R., et al. 2008, ApJ, 686, 1056

Sloan, G. C., Kraemer, K. E., McDonald, I., et al. 2016, ApJ, 826, 44

Sloan, G. C., Lagadec, E., Kraemer, K. E., et al. 2015, in *Why Galaxies Care about AGB Stars III*, ed. F. Kerschbaum, J. Hron, & R. Wing, ASP Conf. Series, 497, 429

Sloan, G. C., Matsuura, M., Lagadec, E., et al. 2012, ApJ, 752, 140

Soszyński, I., Udalski, A., Szymański, M. K., et al. 2009, AcA, 59, 335

Spano, M., Mowlavi, N., Eyer, L., et al. 2011, A&A, 536, 60

Srinivasan, S., Boyer, M. L., Kemper, F., et al. 2016, MNRAS, 457, 2814

Vassiliadis, E., & Wood, P. R. 1993, ApJ, 413, 641

Wells, M., Pel, J.-W., Glasse, A., et al. 2015, PASP, 127, 646

Whitelock, P. A., Menzies, J. W., Feast, M. W., et al. 2009, MNRAS, 394, 795

Wickramasinghe, N. C., Donn, B. D., & Stecher, T. P. 1966, ApJ, 146, 590

Woitke, P. 2006, A&A, 452, 537

Werner, M. W., Roellig, T. L., Low, F. J., et al. 2004, ApJS, 154, 1

Wright, E. L., Eisenhardt, P. R. M., Mainzer, A. K., et al. 2010, AJ, 140, 1868

Wright, G. S., Rieke, G. H., Glasse, A., et al. 2023, PASP, 135, 048003

Yamashita, Y. 1975, Ann. Tokyo Astron. Obs. 15, 47

Zaritsky, D., Harris, J., Thompson, I. B., & Grebel, E. K. 2004, AJ, 128, 1606